MODELING STABILITY OF MAGNETARS AND ACCOMPANYING INTERNAL MAGNETIC FIELDS WITH APPLICATIONS TO CONTINUOUS GRAVITATIONAL WAVE DETECTION

By

Samuel George Frederick II

A THESIS

Submitted to
Davidson College
in partial fulfillment of the distinction of

Honors in the Major – Physics

2019

APPROVAL

The thesis of Samuel G. Frederick II is approved:

Dr. Kristen Thompson — Date
Research Advisor

Dr. Michelle Kuchera — Date
Research Advisor

Dr. Mario Belloni — Date
Department Chair

ABSTRACT

MODELING STABILITY OF MAGNETARS AND
ACCOMPANYING INTERNAL MAGNETIC FIELDS WITH
APPLICATIONS TO CONTINUOUS GRAVITATIONAL WAVE DETECTION

By

Samuel George Frederick II

Possessing the strongest magnetic fields in the Universe, a group of rapidly rotating pulsars known as magnetars mark an extremum of our understanding of physical phenomena. The strength of their magnetic fields is sufficient to deform the shape of the stellar surface, and when the rotational and magnetic axes are not aligned, these deformations lead to the production of gravitational waves (GWs) via a time-varying quadrupole moment. Such gravitational radiation would differ from signals presently detectable by the Laser Interferometer Gravitational-Wave Observatory (LIGO), as these signals would be continuous rather than the momentary "chirp" waveforms of past LIGO inspiral binary merger detections. Here, we construct a computational model for magnetar stellar structure with strong internal magnetic fields. We implement an $n = 1$ polytropic equation of state (EOS) and adopt an existing mixed poloidal and toroidal magnetic field model constrained by the choice of EOS [1]. We utilize fiducial values for magnetar magnetic field strength and various stellar physical attributes. Via computational simulation, we measure the deformation of magnetar stellar structure to determine upper bounds on the strength of continuous gravitational waves as a result of these deformations inducing non-axisymmetric rotation. We then compute upper limits for gravitational wave strain predictions for sources in the McGill Magnetar Catalog, a index of all detected magnetars [2]. This work seeks to inform the sensitivity of future iterations of GW detectors such as Advanced LIGO, and the proposed Einstein Telescope and Laser Interferometer Space Antenna (LISA) to continuous GW signals resulting from magnetars. Detection of these signals would provide key insight into the extreme structure of these stars, and potentially inform our understanding of the highly-dense physical environment of the Universe shortly following the Big Bang.

ACKNOWLEDGMENTS

Writing this statement two short weeks before graduation, I am moved to reflect upon all those which have supported the completion of this thesis, and more broadly, the academic fulfillment of these past four years at Davidson.

This thesis would not have been possible without the support, encouragement, and patience of my co-advisors Dr. Michelle Kuchera and Dr. Kristen Thompson. They each provided countless hours of invaluable feedback and, perhaps more important still, remain endlessly supportive mentors.

I extend sincere appreciation to members of the Davidson Physics Department, both faculty and students, who have provided both insight and assistance. I am deeply grateful for your contributions, and for fostering an exceptional environment of learning over these past four years.

This work builds off a thesis completed by former Duke undergraduate Emily Kuhn, and I wish to fully acknowledge her work as a crucial starting point. We adopt similar methods, including a stellar model based on the $n = 1$ polytrope and utilize both the `PLUTO` and `VisIt` software packages, although we develop independent code and simulations, adopt alternative magnetic field expressions, and pursue different avenues of analysis.

Finally, I am deeply grateful for the continued and abiding support of my family, which made the completion of this thesis realizable.

A passion and enthusiasm for physics, while engaging the emotional rather than the largely-encompassing analytical mindset of science, nonetheless personally offers a deeply essential drive in the pursuit of scientific knowledge. Therefore, I close with a quote from *Cosmos* by Carl Sagan, whose various work forms both a treatise of scientific principles and a moving illustration of the altogether subtle yet profound connection between the elemental ardor of humanity, the pursuit of scientific knowledge, and the Cosmos at large:

> "We wish to pursue the truth no matter where it leads — but to find the truth, we need imagination and skepticism both. We will not be afraid to speculate, but we will be careful to distinguish speculation from fact. The Cosmos is full beyond measure of elegant truths; of exquisite interrelationships; of the awesome machinery of nature."

TABLE OF CONTENTS

LIST OF TABLES

LIST OF FIGURES

CHAPTER 1

ASTROPHYSICS BACKGROUND

Magnetars belong to a group of stellar objects known as pulsars. The stellar structure of pulsars is highly compact and dense, leading to a composition almost entirely of neutrons, fittingly referred to as neutron stars. Together, these stellar objects form a group characterized by remarkable physical attributes including the strongest magnetic fields in the universe, rapid rotation accelerating stellar structure in the relativistic regime, and immense internal densities and pressures which lead to phenomena such as superfluidity of nucleons. Here, we provide explanation of the principle physics underlying this group of stellar objects including their classification, structural regions, magnetic field structure, and further key attributes.

1.1 Properties of Neutron Stars

1.1.1 Description and History

The extreme physical environments modeled in this thesis simulate the structure of neutron stars. These stars form the central physical structure of pulsars and magnetars, making them a logical starting point in our discussion of such stellar objects. The dramatic nature of neutron stars, characterized by densities as high as 10^{15} g·cm^{-3} and pressures exceeding 10^{36} dyn·cm^{-2}, offers a key opportunity for rigorously investigating physical theories under superlative circumstances [3].

By the mid-1960s, considerable progress was made in describing the theoretical structure of neutron stars; however, direct detection remained unresolved. Numerous hypotheses were posed suggesting potential means of observation, often based on established theory regarding the thermal radiation of neutron stars. Given an approximate surface temperature of $\sim 10^6$ K, neutron stars emit blackbody radiation which peaks in the X-ray regime. Among the earliest attempts at X-ray astronomy, initial experimental efforts to detect neutron stars were inconclusive [3]. The discovery and verification of these stars would not come from outright detection of their thermal properties,

but rather from the detection of periodic radio pulses corresponding to the emission and rapid rotation of a pulsar.

FIGURE 1.1: Jocelyn Bell Burnell circa 1976 [4].

In August of 1967, Jocelyn Bell Burnell, a graduate student supervised by Anthony Hewish, detected a curious signal she described as a "bit of scruff" from a radio antenna array intended for studying scintillation of radio sources due to interaction with solar wind [5]. Further detection under higher resolution determined that the signal was periodic and highly stable. Although initial theories to explain the periodicity attributed the signal to the oscillation of white dwarfs or neutron stars, Gold (1968) posited an alternative theory that such a signal may result from the rapid rotation of a magnetized neutron star [3]. Later that year, successful detection of the pulsar associated with the Crab Nebula determined the star's rotational period to be 0.0333 s. This discovery signaled the end to debate over models attributing the source to white dwarf oscillations; these stars are a few orders of magnitude larger than neutron stars and possess lower densities. Given the physical attributes of white dwarfs, these stars can not sustain such high rotational periods without disintegrating. Ultimately, Gold's theory of rapidly rotating, magnetized neutron stars emerged consistent with observation and theoretical constraints.

1.1.2 Formation

Neutron stars form during supernovae. Near the end of the stellar life of a massive ($\gtrsim 8\ M_\odot$) giant or supergiant progenitor star, the fusion process ceases for lighter elements such as hydrogen and helium, transitioning to the fusion of heavier elements including carbon and oxygen supported by high temperatures near the core. This process results in the generation of even heavier elements including silicon, whereby elements form layered regions with heavier material closer to the core. Fusion continues for heavier elements such as silicon; however, this process can not continue forever, as the difference in binding energy between successive nuclei decreases to a critical

point. As silicon fuses into iron, more energy is required for fusion to occur than is released. An endothermic process known as *photodisintegration* occurs, annihilating heavier nuclei and removing an immense amount of thermal energy from regions near the core. Simultaneously, free electrons which previously supported the star via degeneracy pressure undergo rapid electron capture,

$$p^+ + e^- \rightarrow n + \nu_e \,, \tag{1.1}$$

with protons freed by photodisintegration. The sudden disintegration of the stellar core and removal of electron degeneracy pressure leaves the star with no way of maintaining hydrostatic equilibrium, causing the core to undergo gravitational collapse, resulting in a cascading implosion of upper stellar regions [5]. This process, known as *core-collapse*, continues until neutron degeneracy pressure balances the gravitational force [3]. For Type II supernovae categorized by the composition of material surrounding the core, rebounding matter is sent out in highly energetic shocks, leaving behind a remnant core; a neutron star [5]. The dramatic formation of these stars results in the sudden emission of many neutrinos and are thought to produce gravitational waves (GWs). The GWs produced by supernovae are further discussed in §**2.1**, although they are not the source of GW emission investigated in this thesis.

1.1.3 Structural Regions

Neutron stars possess densities and pressures far exceeding most stellar environments. Considering the volume of the star to be roughly fixed, high particle densities in the stellar interior must lead to high occupation numbers, or the mean number of particles crowding a particular state. Under such circumstances, the number of available states is no longer overwhelmingly larger than the number of particles, and the mathematical structure of Maxwell-Boltzmann statistics breaks down. Consequently, neutron star models must consider the role of quantum statistics and relativistic particles in determining stellar pressure and mass density [6]. Subsequent discussion relates these variables via an *equation of state* (EOS), a requirement for constructing neutron star models in

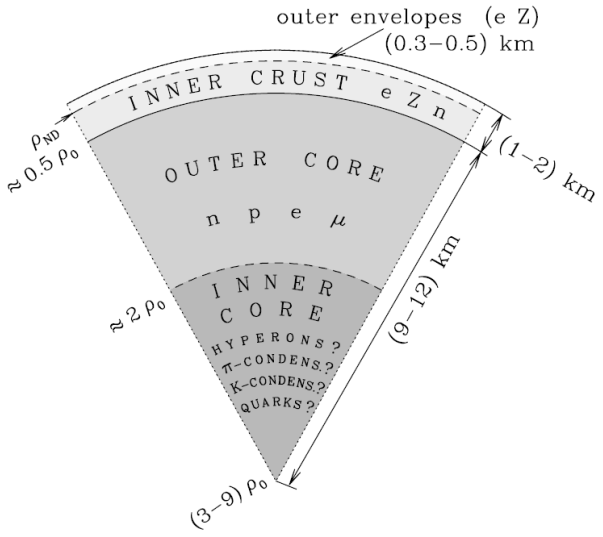

FIGURE 1.2: Schematic of neutron star structural regions [3]. In §**1.1.3**, the "outer envelope" is referred to as the outer crust. The density ρ_0 is referred to as the normal nuclear density, $\sim 2.8 \times 10^{14}$ g·cm^{-3}, the mass density of nucelon matter.

order to describe the numerous formational zones of such stars. For now, we limit our discussion to describing these structural regions within neutron stars.

The outer crust possesses densities ranging from a few g·cm^{-3} up to $\rho \sim 4 \times 10^{11}$ g·cm^{-3}. Strong electron degeneracy provides much of the pressure in this region, and for densities exceeding $\rho \sim 10^6$ g·cm^{-3}, electrons become relativistic. These energetic electrons allow for the conversion of protons to neutrons in crustal iron nuclei via the process of electron capture (1.1). This process results in neutron-rich nuclei, and we may expect the standard process of β-decay,

$$n \rightarrow p^+ + e^- + \bar{\nu}_e \, , \tag{1.2}$$

to revert neutrons to protons within such nuclei. However, due to near complete electron degeneracy resulting in electrons crowding the ground state, emitted electrons via the β-decay process would have no vacant state to occupy, and thus impede decay. This results in the *neutronization* of nuclei, producing a sequence of increasingly neutron-rich elements [5].

The inner crust begins at densities of approximately $\rho \sim 4 \times 10^{11}$ g·cm^{-3} and extends up to $\rho \sim 2 \times 10^{12}$ g·cm^{-3}. Sufficiently high densities result in a minimum energy configuration for neutrons which is located outside the nucleus. This phenomenon is known as neutron drip, whereby

free neutrons emerge. A curious feature of this process is the spontaneous pairing of degenerate neutrons, which was first theorized for electrons in 1957 by Bardeen, Cooper, and Schrieffer (BCS) and subsequently extended to nucleons by Bohr et al. (1958). BCS theory results in the pairing of electrons via a weak attraction due to the electron-phonon interaction [3]. These fermion pairs are referred to as Cooper pairs. Each pairing forms a boson which is free from the restrictions of the Pauli exclusion principle, allowing every neutron pair to assume the lowest energy state. This process forms a superfluid with no resistance [5].

The outer core is characterized by densities ranging from $\rho \sim 2 \times 10^{12}$ g·cm^{-3} up to $\rho \sim 4 \times 10^{14}$ g·cm^{-3}. For densities near $\rho \sim 4 \times 10^{12}$ g·cm^{-3}, neutron degeneracy pressure overtakes electron degeneracy pressure. As a result, nuclei dissolve and structure in this region takes the form of a fluid of free protons, neutrons, and electrons. The cooper pairing of protons and neutrons with constituent particles dominates this region. These pairs form superfluids, for which protons form a superconducting fluid free from ohmic dissipation, or energy lost to resistive heating [5][3].

The inner core and subsequent regions approaching $\rho \sim \rho_{core}$ are subject to active research, and several competing hypotheses exist regarding the formation of exotic and sub-nuclear particles in this region such as the appearance and condensation of hyperons (a class of heavy and unstable baryonic matter), pions, and quark matter. Since laboratory conditions cannot recreate environments sufficient to replicate the inner core, the EOS regarding neutron star cores remains unknown, and thus poses one of the key areas of ongoing research in constructing neutron star models.

1.1.4 Rapid Rotation

In addition to extreme structural properties, neutron stars exhibit rapid rotation. Although progenitor supergiants responsible for the formation of neutron stars may rotate slowly, the collapse of their iron-rich core into a newly formed neutron star must be subject to the conservation of angular momentum. Consequently, even initially slight progenitor core rotation may result in a rapidly rotating neutron star [5]. We consider a classical example for which a progenitor supergiant possess a rotating core with angular frequency ω_i and where we approximate its moment of inertia by

treating the core as a sphere such that $I_i = \frac{2}{5} M_i {R_i}^2$. After core collapse, the neutron star must have angular frequency ω_f. In keeping with our approximation, we assign the neutron star a similar moment of inertia, $I_f = \frac{2}{5} M_f {R_f}^2$. Via conservation of angular momentum, we require

$$I_i \omega_i = I_f \omega_f \rightarrow M_i {R_i}^2 \omega_i = M_f {R_f}^2 \omega_f \ . \tag{1.3}$$

Solving for ω_f, we find

$$\omega_f = \omega_i \left(\frac{R_i}{R_f} \right)^2 \tag{1.4}$$

Astrophysicists often reference the rotational period, P, when referring to rapidly rotating neutron stars. We can express (1.2) in terms of rotational period as

$$P_f = P_i \left(\frac{R_f}{R_i} \right)^2 \tag{1.5}$$

Authors Carrol and Ostile show that for a model involving a progenitor iron core with rotational period P_{core} and resulting neutron star with period P_{ns}, expression (1.3) gives

$$P_{ns} \approx 3.8 \times 10^{-6} \ P_{core} \text{ [5].} \tag{1.6}$$

Clearly, we expect newly formed neutron stars to have remarkably short rotational periods.

1.2 Pulsars

1.2.1 The Pulsar Model

Pulsars are rapidly rotating neutron stars possessing strong dipole magnetic fields. Along magnetic field lines, electrons are accelerated at relativistic velocities, producing synchrotron radiation as the moving charges trace out helical paths. Near the magnetic axis, emission cones along both poles emit focused beams of electromagnetic radiation.

If the magnetic axis is not aligned with the rotational axis of the star, the beam sweeps out a circular path as the star rotates. If there exists a point in the star's rotation during which the beam aligns with the line of sight for an observer on Earth, the beam, and thus the star, is detected as a momentary electromagnetic pulse. These pulses are predominantly received in the radio regime, broadly ranging in frequency from 20 MHz to 10 GHz [5].

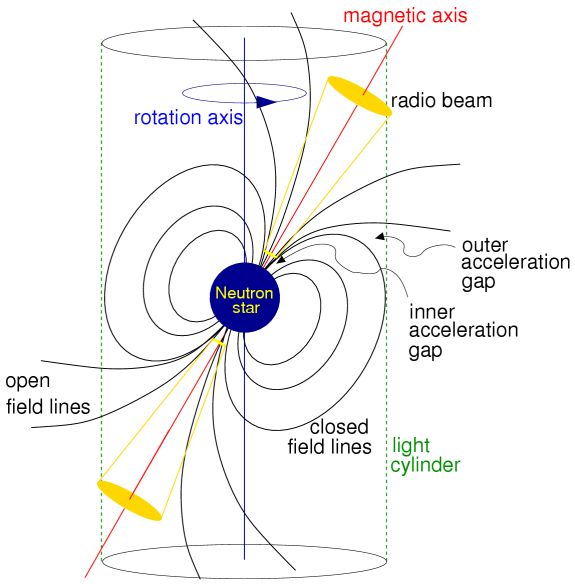

FIGURE 1.3: Schematic of a conventional pulsar [7].

1.2.2 Magnetic Field Amplification

Owing their discovery to electromagnetic radiation induced by the strength of their magnetic fields, most pulsars possess surface magnetic field strengths on the order of $B \sim 10^{11}$–10^{13} G (gauss); however, as we discuss in §**1.3**, exceptional species such as magnetars possess field strengths which exceed this range [3]. Pulsars are believed to have inherited magnetic field configurations from their progenitor stellar origin. Under gravitational collapse, these progenitor fields are amplified as magnetic flux is conserved. To illustrate this phenomena and compare initial and final field strength, we follow a procedure analogous to that of §**1.1.4**. Recall that magnetic flux is defined as

$$\Phi = \int_S \mathbf{B} \cdot dA \ , \tag{1.7}$$

where we represent the surface of the progenitor iron core and newly formed neutron star as $4\pi R_i^2$ and $4\pi R_f^2$, respectively. Furthermore, we consider the magnetic field to be perpendicular to the surface at each point for initial and final configurations, and that the magnitudes B_i and B_f are constant over respective surfaces. Imposing these restrictions, we equate initial and final flux configurations as

$$B_i 4\pi R_i^2 = B_f 4\pi R_f^2 \ . \tag{1.8}$$

For a measure of B_i, we adopt constraints imposed by Carrol and Ostlie for a similar calculation of the relationship between initial and final magnetic field strength for neutron stars[5]. The field strength of the progenitor iron core can be approximated to an upper limit by the strongest observed white dwarf magnetic field, where we express $B_i = B_{wd} \approx 5 \times 10^8$ G. Given that these stars form from the core of a progenitor star with masses slightly less than what is necessary for gravitational collapse to overcome electron degeneracy pressure and thus form a neutron star, they represent a fair approximation for estimating the core radius R_i and magnetic field strength B_i of a progenitor iron core. For $R_i = R_{wd}$, we adopt the value of 7000 km or 7×10^8 cm, and a value of 10 km or 1×10^6 cm is customary for the radius of a neutron star, $R_f = R_{ns}$ [8][3]. Via equation (1.8), we express B_f as

$$B_f = B_{ns} \approx B_{wd} \left(\frac{R_{wd}}{R_{ns}} \right)^2 . \tag{1.9}$$

Plugging in values for parameters that we have specified, we find

$$B_{ns} \approx (4.9 \times 10^5) B_{wd} , \tag{1.10}$$

or that

$$B_{ns} \lessapprox 2.45 \times 10^{14} \text{ G}. \tag{1.11}$$

Because this model depends on an upper-limit estimate for the magnetic field strength of a progenitor iron core, our result somewhat overestimates field strengths typically associated with most neutron stars. However, expression (1.10) provides telling indication of the field strength amplification which occurs in the formation of neutron stars.

1.3 Magnetars

Although the magnetic field strengths derived in expression (1.11) are not observed in the majority of pulsars, such field strengths lie within physically allowed values. Indeed, magnetic field strengths of magnitude $B \sim 10^{14}$–10^{15} G characterize a group of pulsars known as *magnetars*. Our discussion up to this point has detailed the formation as well as the structural and physical properties of neutron stars and pulsars, all attributes which magnetars share. Despite strong magnetic fields,

the EOS for magnetar stellar structure is similar to that for conventional pulsars with weaker field strengths[9]. Therefore, the internal structure of magnetars is consistent with prior discussion of neutron star structure.

The strength of such magnetic fields does however have an appreciable effect on the rotational period (P) of magnetars. Magnetic dipole radiation induces a braking torque $\mathcal{N}$ acting on rotating neutron stars, where

$$\mathcal{N} = -\frac{2\Omega^3 B_{\text{eff}}^2 R^6}{3c^3} = I\dot{\Omega}\,, \tag{1.12}$$

and Ω is the rotational frequency, I is the stellar moment of inertia, $B_{\text{eff}} = B_{eq}\sin\theta$ where B_{eq} is the magnitude of the magnetic field at the equator and θ is the angle between the magnetic and spin axes, and R is the stellar radius [3]. Via equation (1.12), we solve for the magnetic field as

$$B_{\text{eff}} = \left(\frac{3Ic^3}{8\pi^2 R^6} P\dot{P}\right)^{1/2} \tag{1.13}$$

Strong magnetic fields thus increase the rotational period P and the spindown rate $\dot{P}$. As a result, magnetars possess slow rotational periods of 5–8 seconds, a dramatic comparison to some pulsar periods measured in terms of milliseconds [3].

The strength of these magnetic fields exerts tremendous magnetic pressure on the outer crust of the star, and the anisotropic distribution of this pressure deforms the star along the magnetic axis. As previously mentioned, the magnetic axis and rotational axis for pulsars, and consequently magnetars, are often inclined relative to each other. Therefore, deformations on the surface rotate non-axisymmetrically. The focus of the next chapter is to discuss this scenario and the resulting production of gravitational waves.

CHAPTER 2

GRAVITATIONAL WAVES

While the Newtonian theory of gravity requires that a gravitational force propagate instantaneously throughout the Universe, Albert Einstein's groundbreaking 1905 discovery of special relativity laid the groundwork for a gravitational theory consistent with the principles of causality and the propagation of information at or below the finite speed of light. In 1915, Einstein reconciled relativity and gravity in a general theory of relativity, the basic principle of which is elegantly encapsulated in a popular quote by the late American theoretical physicist John A. Wheeler [10]:

> Spacetime tells matter how to move
> Matter tells spacetime how to curve

Perturbations to spacetime in this general theory of relativity propagate at the speed of light, and are referred to as gravitational waves (GWs).

2.1 Signal Sources and Production

Presently, GW signals have only been detected from binary black hole and neutron star mergers [11]. Although these events are dramatic examples of GW production, they potentially constitute a small fraction of a broader range of sources. GW signals can be divided into three categories: binary inspiral mergers, bursts from events such as supernovae, and continuous signals resulting from the rotation of asymmetric sources [12]. The GWs investigated in this thesis are continuous signals, as they result from the rapid rotation of neutron stars with surface deformations induced by the strength of the magnetic field. The inclination of the magnetic axis from the rotational axis allows non-axisymmetric rotation, thus inducing a time-varying gravitational quadrupole.

Gravitational quadrupoles play a similar role in general relativity as dipoles play for electromagnetism. Analogous to how an oscillating dipole produces electromagnetic radiation, a time-varying quadrupole generates gravitational radiation. The reason gravitational quadrupoles, and not dipoles or monopoles, provide the source of gravitational radiation comes from a set of conservation laws.

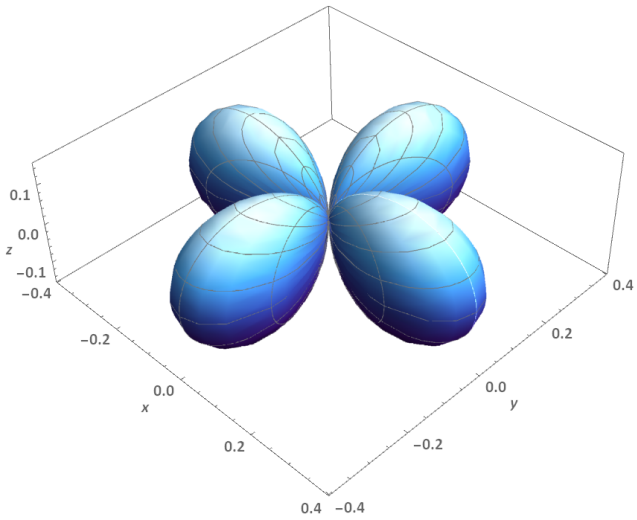

FIGURE 2.1: Quadrupole resulting from the $l = m = 2$ spherical harmonic.

Again, the analogy of electromagnetism provides a useful heuristic tool. Electromagnetic radiation has no monopole component as charge is conserved. Analogously, gravitational radiation has no monopole component because mass is conserved. Furthermore, gravitational dipole radiation is not observed because of the conservation of angular momentum [13].

Over the next few sections, we overview the mathematics of general relativity underlying the theory of gravitational waves in order to provide a basis for subsequent discussion. In §**2.5**, we show that for gravitational waves, the Einstein field equation can be expressed as a wave equation. In §**2.6**, we show that general solutions to this wave equation can take the form of a plane wave, and that this wave propagates at the speed of light. We culminate our discussion by showing in §**2.6** that these waves can be expressed given two distinct polarization states which arise from the time-varying quadrupole discussed earier. These polarization states are key to GW detection, and form a necessary foundation for subsequent discussion of GW signals.

2.2 Linearized Weak-Field Theory

Although GWs result from the dynamics of highly energetic phenomena involving strong fields, their comparatively weak strength allows us to represent them as a small perturbation to flat Minkowski spacetime. Symbolically, we express this near Minkowskian metric as

$$g_{\mu\nu} = \eta_{\mu\nu} + h_{\mu\nu} \,, \tag{2.1}$$

where, as convention, $\eta_{\mu\nu}$ represents the flat Minkowski spacetime metric of special relativity and $h_{\mu\nu}$ represents the perturbation we wish to impose. This expression illustrates that instead of considering the flat spacetime of the Minkowski metric, we are considering a slightly curved spacetime $g_{\mu\nu}$. Subsequent discussion allows a reinterpretation of this metric following additional establishing principles. The notion of applying a small perturbation to flat Minkowski space is considered a *linearized theory of gravity*, as we wish to keep only first order terms in $h_{\mu\nu}$, where $|h_{\mu\nu}| \ll 1$ [10].

To remain consistent with a key tenant of general relativity, we require that our near Minkowskian metric hold under any number of coordinate systems and transformations. Specifically, our metric must transform properly under global Lorentz transformations and infinitesimal general coordinate transformations [14].

We can express a global Lorentz transform from one coordinate system, x^{μ}, to the transformed coordinate system, $x^{\mu'}$, as

$$x^{\mu} \rightarrow x^{\mu'} = \Lambda^{\mu'}_{\nu} x^{\nu} \,, \tag{2.2}$$

where Λ is the Lorentz transformation of special relativity. An important feature of these transformations is that when acted upon the Minkowski metric, they preserve its invariance,

$$\eta_{\mu\nu} = \Lambda^{\rho}_{\mu}\Lambda^{\sigma}_{\nu}\eta_{\rho\sigma} \,, \tag{2.3}$$

for the dummy variables ρ and σ. We apply the global Lorentz transformation to our metric, $g_{\mu\nu}$, to show that the transformation of the metric is

$$g'_{\mu\nu} = \Lambda^{\rho}_{\mu}\Lambda^{\sigma}_{\nu}(\eta_{\rho\sigma} + h_{\rho\sigma}) \,, \tag{2.4}$$

and via equation (2.3), we see

$$g'_{\mu\nu} = \eta_{\mu\nu} + \Lambda^{\rho}_{\mu}\Lambda^{\sigma}_{\nu} h_{\rho\sigma} \,. \tag{2.5}$$

This establishes the transformed metric $g'_{\mu\nu}$ is of the same form as equation (2.1), and that

$$h'_{\mu\nu} = \Lambda^{\rho}_{\mu}\Lambda^{\sigma}_{\nu} h_{\rho\sigma} \,. \tag{2.6}$$

Thus, we see our metric transforms as

$$g_{\mu\nu} = \eta_{\mu\nu} + h'_{\mu\nu} \, . \tag{2.7}$$

Equations (2.6) and (2.7) establish that $h_{\mu\nu}$ transforms like the components of a tensor on flat spacetime. In other words, $h_{\mu\nu}$ is a Lorentz tensor. It is worth noting the importance of this conclusion. Since $h_{\mu\nu}$ acts like a tensor in Minkowski spacetime, our conception of $g_{\mu\nu}$ itself can be modified. Rather than considering the metric as representing slightly curved spacetime, we may refer to $h_{\mu\nu}$ as a tensor field defined on flat Minkowski spacetime and thus can be considered a special relativistic gravitational field [14].

As we wish to keep only the first order terms of $h_{\mu\nu}$, the metric inverse $g^{\mu\nu}$ can be expressed as

$$g^{\mu\nu} = \eta^{\mu\nu} - h^{\mu\nu} \, , \tag{2.8}$$

where we require $g^{\mu\nu} g_{\nu\sigma} = \delta^{\mu}_{\sigma}$ and allow the raising and lowering of indices via the Minkowski metric $\eta^{\mu\nu}$ such that the rank-2 and rank-1 contravarient perturbation tensors are

$$h^{\mu\nu} = \eta^{\mu\rho} \eta^{\nu\sigma} h_{\rho\sigma} \, , \tag{2.9}$$

and

$$h^{\mu}_{\nu} = \eta^{\mu\rho} h_{\sigma\rho} \, , \tag{2.10}$$

respectively.

2.3 The Linearized Einstein Equations

So far, we have shown some of the properties of the metric tensor, $g_{\mu\nu}$, how it is preserved under Lorentz transformations and the resulting interpretation of $h_{\mu\nu}$, and the existence of the metric inverse. In order to describe how the curvature of spacetime induced by the metric $g_{\mu\nu}$ interacts with matter, we require a set of field equations, similar to the way in which Maxwell's equations provide field equations for electromagnetism [14]. The Einstein equations provide a basis for our analysis,

$$R_{\mu\nu} - \frac{1}{2} R g_{\mu\nu} = \frac{8\pi G}{c^4} T_{\mu\nu} \, , \tag{2.11}$$

where $R_{\mu\nu}$ is the Ricci tensor, R is the Ricci scalar, $g_{\mu\nu}$ is our familar metric, and $T_{\mu\nu}$ is the energy-momentum tensor [15]. Although the Einstein equations are non-linear, we seek a linearized approximation of these equations which fits our metric. Following the approach of Cheng, Maggiore, and Hobson ([10]), we determine the Riemann curvature tensor to linear order

$$R_{\alpha\mu\beta\nu} = \frac{1}{2}(\partial_\alpha\partial_\nu h_{\mu\beta} + \partial_\mu\partial_\beta h_{\alpha\nu} - \partial_\alpha\partial_\beta h_{\mu\nu} - \partial_\mu\partial_\nu h_{\alpha\beta}) \,, \tag{2.12}$$

which in turn determines the Ricci tensor

$$R_{\mu\nu} = \eta^{\alpha\beta} R^{(1)}_{\alpha\mu\beta\nu} = \frac{1}{2}(\partial_\alpha\partial_\nu h^\alpha_\mu + \partial_\mu\partial_\alpha h^\alpha_\nu - \Box h_{\mu\nu} - \partial_\mu\partial_\nu h) \,. \tag{2.13}$$

We also find the Ricci scalar to be

$$R = \partial_\mu\partial_\nu h^{\mu\nu} - \Box h \,, \tag{2.14}$$

where $\Box$ is the D'Alembertian operator as defined on Minkowski space as

$$\Box = g^{\mu\nu}\partial_\mu\partial^\mu = \frac{1}{c^2}\frac{\partial^2}{\partial t^2} - \frac{\partial^2}{\partial x^2} - \frac{\partial^2}{\partial y^2} - \frac{\partial^2}{\partial z^2} \,, \tag{2.15}$$

and where we assume the convention $(-,+,+,+)$ for the Minkowski metric signature. Furthermore, $h = h^\mu_\mu$ is the trace, or the sum of the diagonal components of the rank-2 tensor [10][15][14]. Our resulting linearized Einstein equation is

$$R_{\mu\nu} - \frac{1}{2}R\eta_{\mu\nu} = \frac{8\pi G}{c^4}T_{\mu\nu} \,. \tag{2.16}$$

2.4 The Infinitesimal Coordinate Change as a Gauge Transformation

Recall our discussion of metric transformations in §**2.2**. We mentioned that our metric must transform under global Lorentz transformations and infinitesimal coordinate transformations. The latter frames the discussion of this subsection, as such coordinate transformations enjoy a gauge freedom in the context of general relativity. Generally speaking, a gauge freedom allows one to impose conditions on quantities or fields which do not affect the interpretation of an accompanying field. By fixing a gauge, we seek to eliminate degeneracy so that our metric, $g_{\mu\nu}$, is uniquely defined

and is independent of the chosen coordinate system [12]. In the context of electromagnetism, gauge freedoms allow for changes in the electric potential, V, and the magnetic vector potential, $\mathbf{A}$, as

$$\mathbf{A}' = \mathbf{A} + \nabla\lambda \tag{2.17}$$

and

$$V' = V - \frac{\partial\lambda}{\partial t}\,, \tag{2.18}$$

where $\nabla\lambda$ and $\partial\lambda/\partial t$ represent modifications via a scalar function $\lambda(\mathbf{r}, t)$ which we are free to impose on $\mathbf{A}$ and V; such modifications affect neither the magnetic field nor the electric field [16].

To determine our gauge transformation, we apply a small shift of the position vector, forming an infinitesimal general coordinate transformation

$$x'^{\mu} = x^{\mu} + \xi^{\nu}\,, \tag{2.19}$$

where ξ^{ν} are four arbitrary functions of the same order of size as $h_{\mu\nu}$. We differentiate equation (2.19) to obtain the transformation for the contravarient components

$$\frac{\partial x'^{\mu}}{\partial x^{\nu}} = \delta^{\mu}_{\nu} + \partial_{\nu}\xi^{\mu}\,, \tag{2.20}$$

where δ^{μ}_{ν} is the Kronecker delta. Equation (2.20) also implies the inverse transformation to first order quantities

$$\frac{\partial x^{\mu}}{\partial x'^{\nu}} = \delta^{\mu}_{\nu} - \partial_{\nu}\xi^{\mu}\,. \tag{2.21}$$

Following a similar procedure as undertaken in equation (2.4), we apply these transformations to the metric tensor:

$$g'_{\mu\nu} = \frac{\partial x^{\rho}}{\partial x'^{\mu}}\frac{\partial x^{\sigma}}{\partial x'^{\nu}} g_{\rho\sigma} = (\delta^{\rho}_{\mu} - \partial_{\mu}\xi^{\rho})(\delta^{\sigma}_{\nu} - \partial_{\nu}\xi^{\sigma})(\eta_{\rho\sigma} + h_{\rho\sigma})\,, \tag{2.22}$$

such that

$$g'_{\mu\nu} = \eta_{\mu\nu} + h_{\mu\nu} - \partial_{\mu}\xi_{\nu} - \partial_{\nu}\xi_{\mu}\,, \tag{2.23}$$

where we concatenate our equation via the expression $\xi_\mu = \eta_{\mu\nu}\xi^\nu$. From equation (2.23) and given the invariance of Minkowski space under transformation, we can express transformation of the metric perturbation as

$$h'_{\mu\nu} = h_{\mu\nu} - \partial_\mu \xi_\nu - \partial_\nu \xi_\mu \,, \tag{2.24}$$

such that our infinitesimal transformation is consistent with the form of equation (2.7) [3][10].

Recall that our resulting expression for $h'_{\mu\nu}$ under Global Lorentz transformations allowed us to view $h_{\mu\nu}$ as a Lorentz tensor acting on Minkowski space. Adopting this interpretation, we may view equation (2.24) as a gauge transformation, where it is valuable to notice the similarities between this equation and expressions (2.17) and (2.18) for electromagnetism.

2.5 The Wave Equation

By choice of gauge, we may simplify the process of calculation to obtain a wave equation in the form of our linearized Einstein equation. This process is analogous to the choice of the Lorenz gauge in electromagnetism to obtain the inhomogenous wave equation, which allows electrodynamics to become entirely an issue of solving such equations [16]. In general relativity, the Lorenz gauge condition is

$$\partial^\mu \bar{h}_{\mu\nu} = 0 \,, \tag{2.25}$$

where $\bar{h}_{\mu\nu}$ is known as the *trace-reversed perturbation*

$$\bar{h}_{\mu\nu} = h_{\mu\nu} - \frac{h}{2}\eta_{\mu\nu} \,, \tag{2.26}$$

which helps to simplify our expression.

We can use our chosen gauge to show that $\partial^\mu h_{\mu\nu} = \frac{1}{2}\partial_\nu h$, such that components of the Einstein field equation (2.11) give the Ricci tensor to be $R_{\mu\nu} = -\frac{1}{2}\Box h_{\mu\nu}$ and the Ricci scalar as $R = -\frac{1}{2}\Box h$. Inserting these relations into our Einstein field equation (2.16), we form the wave equation

$$\Box \bar{h}_{\mu\nu} = \frac{16\pi G}{c^4} T_{\mu\nu} \,. \tag{2.27}$$

Therefore, linearized perturbations of Minkowski spacetime adhere to a wave equation, motivating the distinction of *gravitational waves*.

2.6 Plane Waves and Polarization States

For the propagation of gravitational waves in a vacuum, we can represent such waves by the superposition of plane wave solutions of the form

$$h_{\mu\nu} = \epsilon_{\mu\nu} e^{ik_\rho x^\rho} \,, \tag{2.28}$$

where $\epsilon_{\mu\nu}$ is the polarization tensor for the gravitational wave. This tensor is composed of constants forming a symmetric tensor such that $\epsilon_{\mu\nu} = \epsilon_{\nu\mu}$ [10].

In a vacuum, the energy-momentum tensor becomes $T_{\mu\nu} = 0$, such that the wave equation (2.27) takes the form

$$\Box \bar{h}_{\mu\nu} = 0 \,. \tag{2.29}$$

The trace of $\bar{h} = -h$ satisfies the same wave equation such that

$$\Box h_{\mu\nu} = 0 \,. \tag{2.30}$$

By substituting equation (2.28) into equation (2.30), we see that

$$k^2 \epsilon_{\mu\nu} e^{ikx} = 0 \,, \tag{2.31}$$

where $k^\alpha = (\omega/c, \vec{k})$ is the four-wavevector such that

$$k^2 = k_\alpha k^\alpha = -\frac{\omega^2}{c^2} + \vec{k}^2 = 0 \,. \tag{2.32}$$

Because the square of the magnitude of k^α is zero, the wavevector is referred to as a null vector. Recall that a wavepacket must have both a phase velocity and a group velocity, where the packet propagates at v_{group}. We compute both velocities:

$$v_{phase} = \frac{\omega}{k} \rightarrow -\frac{\omega^2}{c^2} + \vec{k}^2 = 0 \rightarrow \frac{\omega}{k} = c \,, \tag{2.33}$$

and

$$v_{group} = \frac{\partial \omega}{\partial k} \rightarrow -\frac{\omega^2}{c^2} + \vec{k}^2 = 0 \rightarrow \omega = c|\vec{k}| \rightarrow \frac{\partial \omega}{\partial k} = c \,. \tag{2.34}$$

Therefore, gravitational waves must propagate at the speed of light, c. A final condition required in order to satisfy the Lorenz gauge condition is that

$$k^{\mu}\epsilon_{\mu\nu} = 0 \,, \tag{2.35}$$

establishing that the polarization tensor must be transverse [10].

The condition (2.35) allows additional gauge freedom as long as the Lorenz gauge, expression (2.25), is preserved. We use this gauge freedom to simplify the polarization tensor such that $\epsilon_{\mu\nu}$ becomes traceless:

$$\epsilon^{\mu}_{\mu} = 0 \,. \tag{2.36}$$

This traceless condition requires that a gravitational wave and its polarization states act with shearing forces which do not result in permanent expansions or contractions as the wave propagates transversely through spacetime [17]. We may further require that

$$\epsilon_{\mu 0} = \epsilon_{0\mu} = 0 \,. \tag{2.37}$$

The choice of these conditions collectively forms what is called the *transverse-traceless gauge*.

Having set additional conditions on the polarization tensor, we shall now determine its form in more detail. Consider a wave propagating purely in the z-direction (x^3). Given that the wavevector is null as established in expression (2.32), k^{α} must take the form

$$k^{\alpha} = \frac{1}{c}(\omega, 0, 0, \omega) \,. \tag{2.38}$$

In order for the wavevector to satisfy the transverse condition (2.35), we require

$$k^3\epsilon_{3\nu} = 0 \rightarrow \omega\epsilon_{3\nu} = 0 \,. \tag{2.39}$$

Recall that the polarization tensor is symmetric such that

$$\epsilon_{3\nu} = \epsilon_{\nu 3} = 0 \,. \tag{2.40}$$

Collectively, these conditions allow only ϵ_{11}, ϵ_{22}, ϵ_{12}, and ϵ_{21} to be non-zero components. Provided the traceless condition (1.36) for the polarization tensor, we require $\epsilon_{11} = -\epsilon_{22}$. Furthermore, the

symmetric condition for $\epsilon_{\mu\nu}$ implies that $\epsilon_{12} = \epsilon_{21}$. We refer to the magnitude of ϵ_{11} and ϵ_{22} as h_+ and the magnitude of ϵ_{12} and ϵ_{21} as $h_\times$. Our metric perturbation then has the form

$$h_{\mu\nu}(z,t) = \begin{pmatrix} 0 & 0 & 0 & 0 \\ 0 & h_+ & h_\times & 0 \\ 0 & h_\times & -h_+ & 0 \\ 0 & 0 & 0 & 0 \end{pmatrix} e^{i\omega(z-ct)/c} \,. \tag{2.41}$$

We see there exist two distinct polarization states:

$$\epsilon^{\mu\nu}_{(+)} = h_+ \begin{pmatrix} 0 & 0 & 0 & 0 \\ 0 & 1 & 0 & 0 \\ 0 & 0 & -1 & 0 \\ 0 & 0 & 0 & 0 \end{pmatrix} \quad \text{and} \quad \epsilon^{\mu\nu}_{(\times)} = h_\times \begin{pmatrix} 0 & 0 & 0 & 0 \\ 0 & 0 & 1 & 0 \\ 0 & 1 & 0 & 0 \\ 0 & 0 & 0 & 0 \end{pmatrix} . \tag{2.42}$$

The magnitude of h_+ and $h_\times$ depend on the axis along which detection is made, making these quantities anisotropic. This is a consequence of the antisotropic nature of the gravitational quadrupole, whose configuration relative to an observer on Earth determines the strength of the h_+ and $h_\times$ polarization modes [18].

2.7 Signal Wave Strain and Ellipticity

We require an expression for the gravitational wave amplitude, or the *wave strain*, which characterizes the maximum amplitude of either polarization state. The slow rotation of magnetars allows us to approximate their spinning by rigid body rotation, leading to the expressions

$$h_+ = h_0 \frac{1 + \cos^2(\iota)}{2} \cos(2\pi f_{\rm gw} t) \tag{2.43a}$$

$$h_\times = h_0 \cos(\iota) \sin(2\pi f_{\rm gw} t) \,, \tag{2.43b}$$

where ι is the angle between the line of sight of the observer and the axis of rotation, and $f_{\rm gw} = 2/P$ is the gravitational wave frequency for P the period of rotation for the star [3][15]. Notice that if $\iota = 0$ rad, both polarization amplitudes are maximized and h_0 represents the sum of the square of each polarization; therefore, h_0 represents the parameter quantifying the wave strain of a GW signal. For a rigid rotating star, h_0 can be expressed in terms of physical constants and variables as

$$h_0 = \frac{4\pi^2 G}{c^4} \frac{I_0 f_{\rm gw}^2}{r} \epsilon \,, \tag{2.44}$$

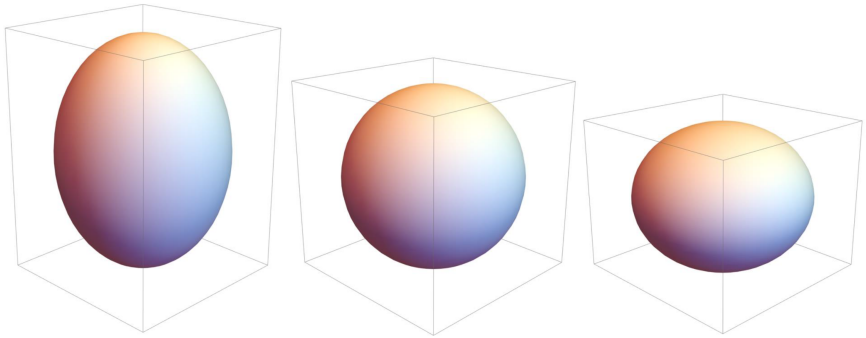

FIGURE 2.2: Three spheroids representing stars of varying ellipticity. From left to right, a prolate spheroid with $\epsilon < 0$, a uniform sphere with $\epsilon = 0$, and an oblate spheroid with $\epsilon > 0$.

where I_0 is the moment of inertia for a spherically symmetric star, and ϵ is a measure of the stellar ellipticity, defined as

$$\epsilon = \frac{I_{zz} - I_{xx}}{I_0} \, . \tag{2.45}$$

We determine I_{zz} and I_{xx} from the inertia tensor,

$$I_{jk} = \int_V \rho(r)\big(r^2\delta_{jk} - x_j x_k\big)dV \, . \tag{2.46}$$

If the stellar ellipticity is negative, meaning $I_{zz} < I_{xx}$, the star is considered *prolate*. Conversely, a positive stellar ellipticity corresponding to $I_{zz} > I_{xx}$ means that the star is considered *oblate*.

From expressions (2.44-2.46), we have shown that measurement of the wave strain, h_0, depends on the degree to which the distribution of mass is spherically non-uniform, i.e, when $I_{zz} \neq I_{xx}$. In the case of neutron stars and magnetars, this means that knowledge of the time evolution of the stellar mass density, $\rho(r)$, due to a strong magnetic field informs measurement of I_{zz} and I_{xx}, and furthermore, measurement of the ellipticity and ultimately wave strain.

The work of this thesis is to construct a stellar model via structural equations such as $\rho(r)$, while also assigning a strong internal magnetic field. Evolution of this computational model provides the necessary means for determining how the magnetic field induces modifications in the density equation from its initial state. In turn, we determine numerical approximations for I_{zz} and I_{xx} throughout the time evolution of our simulation, where we anticipate approximate stability to eventually be achieved for these inertia tensor component's numerical values. We expect that, although these values might change rapidly during the initial stages of the simulation, values

for I_{zz} and I_{xx} may asymptotically approach stable values as the simulation evolves. Therefore, our intention is to run simulations of stellar structure to such a time as asymptotic stability is approximately achieved for the inertia tensor components of interest. Such a procedure allows us to determine estimates for quantifying the wave strain of continuous gravitational waves resulting from the stellar surfaces of magnetars as induced by the rotationally non-axisymmetric deformations due to the strength of the star's internal magnetic field.

Having established the theoretical motivations for constructing a magnetar stellar model, we now turn to discussion of structural equations, including the determination of $\rho(r)$, required for producing physically stable and representative models.

CHAPTER 3

STELLAR STRUCTURE MODEL

3.1 Newtonian Structural Equations

3.1.1 Hydrostatic Equilibrium

The construction of a stellar model at static equilibrium requires a crucial balancing of forces acting upon the stellar interior. Specifically, the force of gravity must be equally opposed; otherwise, gravitational collapse quickly brings the stellar system out of equilibrium. The equation of hydrostatic equilibrium

$$\frac{dP}{dr} = -G\frac{M_r \rho}{r^2} \, , \tag{3.1}$$

where M_r is the mass interior to the radius r for $r < R_{\text{star}}$, provides the basis for balancing the gravitational force with structural variation throughout the stellar interior [5]. The change in the pressure must counteract the inward force due to gravity. We see that as r increases, the sign of the change in pressure is strictly negative; pressure must decrease with increasing radius.

3.1.2 Mass Conservation

The equation for hydrostatic equilibrium hints at the notion that we require an an additional equation to describe the change of mass in the stellar interior, given M_r must change with radius. Such an expression comes in the form of the mass conservation equation,

$$\frac{dM_r}{dr} = 4\pi r^2 \rho \, . \tag{3.2}$$

When given an expression for density $\rho(r)$, we may solve for the stellar mass M via separation of variables and integration [5].

3.2 The Equation of State

The time-independent equations of hydrostatic equilibrium and mass conservation provide necessary structural equations for describing stable and physical stellar systems. However, for the purpose of constructing stellar models, an additional equation, an *equation of state* (EOS), relating pressure to a number of state variables describing stellar structure is required. Initially, this statement may seem vague; however, a considerable degree of freedom exists in choosing an EOS, and in comparing such equations, each may be a function of a varying number of stellar variables such as density, temperature, neutron number density, etc. The extent of such parameterizations depend of the stellar structure which is to be modeled.

3.2.1 Polytropes: General Solutions

Equations of state which parameterize pressure exclusively as a function of density are known as *polytropes*. Their functional form can be expressed as

$$P(\rho) = K\rho^{\gamma} \ , \tag{3.3}$$

where γ is often represented by the *polytropic index n* via

$$\gamma = \frac{n+1}{n} \ . \tag{3.4}$$

Then, polytropes can be classified by the chosen value for n as

$$P(\rho)_n = K\rho^{\frac{n+1}{n}} \ , \tag{3.5}$$

where K is the *polytropic constant* [5].

3.2.2 The N = 1 Polytrope

Equations of state are often categorized by the compressibility of stellar matter, where a lower adiabatic index (3.4) corresponds to lower compression and vice versa [3]. This implies that the

structural composition of the stellar interior sets a constraint on representative equations of state. Under this consideration, we implement an $n = 1$ polytropic EOS in modeling neutron star structure.

Prior work has established neutron star structure as well approximated by the choice of polytropic EOS corresponding to $(0 < n \lesssim 1)$ [19][20][12]. As we shall discuss in §**3.2.3**, an expression for density as a function of radius can be determined via solutions to the *Lane-Emden* equation (3.12). There exist only three analytic solutions to this equation, specifically for $n = 0$, 1, and 5. Therefore, the $n = 1$ polytrope has the added benefit of the following analytic solutions for $\rho(r)$ and $P(r)$ from which stellar structure can be entirely determined:

$$\rho(r) = \rho_c \frac{\sin(\pi r/R)R}{r\pi}, \quad \text{for } r < R \tag{3.6a}$$

$$P(r) = K\rho(r)^2 . \tag{3.6b}$$

Although the analytic nature of this solution provides a convenience in computation and modeling, more importantly, we adopt this model with further consideration for the volume of existing literature. Specifically, as we show in Chapter 4, stellar magnetic field model configurations are constrained by the choice of EOS [1]. Whereby analytic expressions for magnetic field models are well determined for the $n = 1$ polytropic EOS, such models allow for ready implementation in our computational model.

For equations (3.6a) and (3.6b), we must specify two constants: the central density ρ_c and the polytropic constant K. Current estimates place ρ_c near $\sim 10^{15}$ g·cm^{-3}, and we adopt the following value based on previous work [3][12]

$$\rho_c = 2.0 \times 10^{15} \text{ g·cm}^{-3}. \tag{3.7}$$

The polytropic constant K can be determined indirectly by utilizing the following relation for stellar radius derived from expressions (3.14) and (3.15) of the Lane-Emden equation

$$R = \alpha_n \xi_1 = \left[\frac{K(n+1)}{4\pi G}\right]^{1/2} \rho_c^{(1-n)/2n} \xi_1 , \tag{3.8}$$

where ξ_1 is defined by $\Theta_n(\xi_1) = 0$, such that ξ_1 is a dimensionless constant parameterizing the radius of the star relative to the density scaling function $\Theta_n(\xi)$ [19]. These functions and their

motivation are discussed in more detail in §**3.2.3**. For the $n = 1$ polytrope, the scaling function takes the analytic form

$$\Theta_1(\xi) = \frac{\sin(\xi)}{\xi} \,, \tag{3.9}$$

such that

$$\Theta_1(\xi_1) = \frac{\sin(\xi_1)}{\xi_1} = 0 \,. \tag{3.10}$$

Notice expression (3.10) corresponds to the first root for the zeroth-order Bessel function, such that $\xi_1 = \pi$. Returning to expression (3.8), we intend to specify a stellar radius R based on accepted values for neutron star radii and rearrange our expression for K. Implementing a stellar radius of 10 km as informed by prior work, we rearrange (3.8) such that the polytropic constant becomes

$$K = \frac{4\pi G}{(n+1)} \left[\frac{R}{\rho_c^{(1-n)/2n} \xi_1} \right]^2 \,. \tag{3.11}$$

For $n = 1$, $R = 10$ km $= 10^6$ cm, and $\xi_1 = \pi$, we find

$$K = \frac{2G}{\pi} \Big[1 \times 10^6 \text{ cm} \Big]^2 \approx 4.246 \times 10^4 \text{ cm}^5 \cdot \text{g}^{-1} \cdot \text{s}^{-2} \,. \tag{3.12}$$

3.2.3 The Lane-Emden Equation

One may have noticed that in discussing the equations for hydrostatic equilibrium and mass conservation, the density as a function of radius, $\rho(r)$, must be specified. In order to determine a radial parameterization of density, we require a differential equation for $\frac{d\rho}{dr}$. Such an expression may be obtained by relating our structural differential equations in conjunction with our chosen polytropic EOS. Notice that if we rearrange equation (3.1) and take a radial derivative, we obtain

$$\frac{d}{dr} \left(\frac{r^2}{\rho} \frac{dP}{dr} \right) = -G \frac{dM_r}{dr} \,. \tag{3.13}$$

The right-hand side of this expression includes the mass conservation relation (3.2), such that we make appropriate substitutions whereby our differential equation becomes

$$\frac{1}{r^2} \frac{d}{dr} \left(\frac{r^2}{\rho} \frac{dP}{dr} \right) = -4\pi G \rho \,. \tag{3.14}$$

The expression is fully in the form of radius, pressure, and density, and we now implement a chosen polytropic EOS, making substitutions for pressure P and density ρ as necessary, and where we make use of expression (3.4), such that we have

$$\left(\frac{n+1}{n}\right)\frac{K}{r^2}\frac{d}{dr}\left[r^2\rho^{(1-n)/n}\frac{d\rho}{dr}\right] = -4\pi G\rho \ . \tag{3.15}$$

We notice that our differential equation now relates density directly to radius. Subsequent transformations serve to simplify the form of this equation; however, such substitutions preserve the functional relation of equation (3.15). It is thereby customary to express density as

$$\rho(r) \equiv \rho_c[\Theta_n(r)]^n \ \text{ where } \ 0 \leq \Theta_n \leq 1 \tag{3.16}$$

such that $\Theta_n(r)$ is a dimensionless and radially dependent equation which scales density in accordance with the core density, ρ_c. Substituting expression (3.9) into expression (3.8), we introduce the additional expressions

$$\alpha_n \equiv \left[(n+1)\left(\frac{K\rho_c^{(1-n)/n}}{4\pi G}\right)\right]^{1/2} \ , \tag{3.17}$$

and the dimensionless variable

$$\xi \equiv \frac{r}{\alpha_n} \ , \tag{3.18}$$

such that we arrive at the *Lane-Emden equation*,

$$\frac{1}{\xi^2}\frac{d}{d\xi}\left[\xi^2\frac{d\Theta_n}{d\xi}\right] = -(\Theta_n)^n \ . \tag{3.19}$$

This equation provides solutions for the dimensionless function $\Theta_n(\xi)$. Via an appropriate change of parameters, one can subsequently obtain expressions for $\rho_n(r)$, and by extension $P_n(r)$ [5]. In turn, these expressions entirely determine stellar structure.

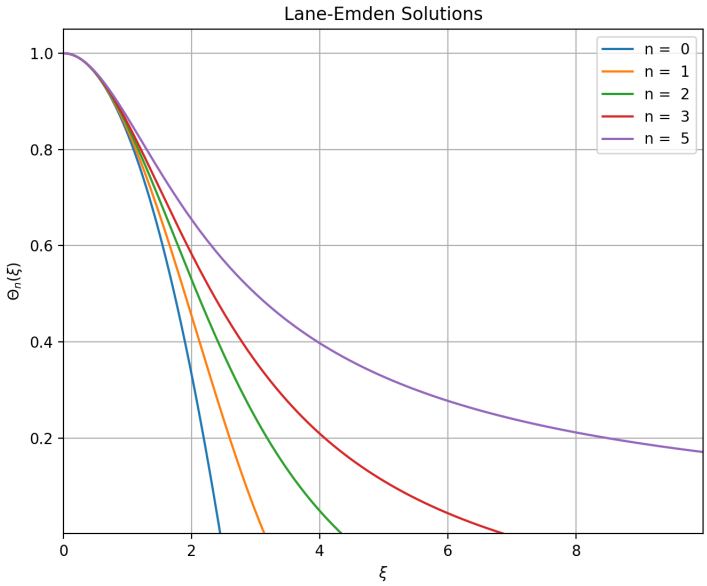

FIGURE 3.1: Solutions to the Lane-Emden equation for $n = 0, 1, 2, 3, 5$. Notice that the asymptotic solution for $n = 5$ results in infinite radius, $\xi_1 = \infty$. Only the solutions corresponding to $n = 0, 1$, and 5 are analytic; all other solutions must be computed numerically.

3.3 The Gravitational Potential

Our discussion has covered methods for obtaining radial expressions for pressure and density, and particular solutions for the $n = 1$ polytrope. Recall that hydrostatic equilibrium requires the balance of an inward gravitational force with the radial change in pressure. It follows that in the process of deriving the Lane-Emden equation, we can reformulate our expression to solve instead for gravitational potential. Thus, expression (3.14) can be written as

$$\frac{1}{r^2}\frac{d}{dr}\left(r^2\frac{d\Phi_g}{dr}\right) = 4\pi G\rho \,. \tag{3.20}$$

This expression is the spherically symmetric form of Poisson's equation for gravitational potential per unit mass, where $\Phi_g \equiv \varphi_g/m$ [5]. We determine solutions to Φ_g as constrained by our determined expression for density, equation (3.6a), which satisfy the following boundary conditions:

$$\frac{d\Phi_g}{dr} = 0 \Big|_{r=0}, \tag{3.21a}$$

$$\Phi_g \Big|_{r=R\ \text{inside}} = \Phi_g \Big|_{r=R\ \text{outside}}, \tag{3.21b}$$

$$\frac{d\Phi_g}{dr} \Big|_{r=R\ \text{inside}} = \frac{d\Phi_g}{dr} \Big|_{r=R\ \text{outside}}. \tag{3.21c}$$

Provided our analytic expression for density of a $n = 1$ polytrope (3.6a), we can use separation of variables and substitution to solve equation (3.20) for Φ_g [12]. We find the following expressions for the gravitational potential, converting Φ_g to $\varphi(r)$ by multiplying through by m in each equation:

$$\varphi_{\text{core}} = 4G\rho_c \left(-\frac{R^2}{\pi} - \frac{M}{4R\rho_c} \right), \qquad \text{for } r = 0 \tag{3.22a}$$

$$\varphi_{\text{inside}}(r) = 4G\rho_c \left(\frac{-R^3 \sin(\pi r/R)}{\pi^2 r} - \frac{M}{4R\rho_c} \right), \qquad \text{for } 0 < r < R \tag{3.22b}$$

$$\varphi_{\text{outside}}(r) = -\frac{GM}{r}, \qquad \text{for } r > R \tag{3.22c}$$

Given that the gravitational potential must be spherically symmetric, we plot the functional form of our potential against radius to globally verify its continuity and adherence to specified boundary conditions within the computational domain.

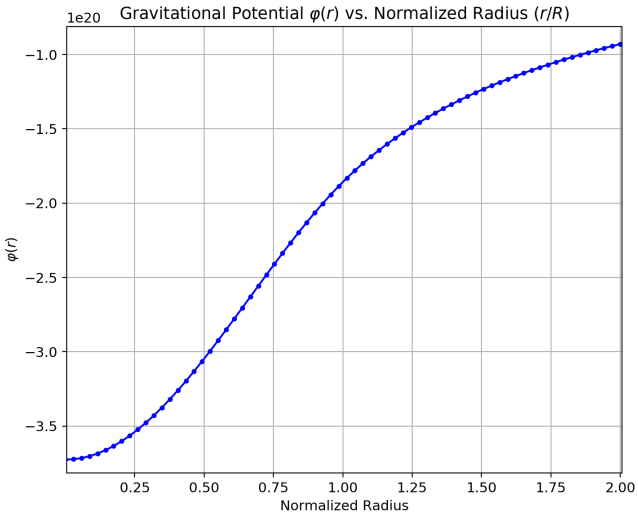

FIGURE 3.2: The piecewise continuous gravitational potential $\varphi(r)$ across all domains interior and exterior to the star. Visual inspection confirms the potential follows set boundary conditions.

It is valuable to note that as the stellar model evolves and the magnetic field changes, the model's gravitational potential remains static; the potential adheres to its form determined here as assigned via initial conditions of the simulation. This approximation, being widely adopted, is referred to as the Cowling approximation, and provides considerable accuracy under direct comparison tests between static and dynamic potentials for modeling stellar structure which, under evolution, is slightly perturbed from initial conditions [21].

CHAPTER 4

MAGNETIC FIELD MODEL

4.1 Hydromagnetic Equilibrium

In chapter 3, we began our discussion with the equation of hydrostatic equilibrium, balancing the radial change in pressure against the inward-seeking force of gravity, ultimately allowing us to construct expressions for stellar density and pressure. In constructing a spherically symmetric model for the magnetic field in the stellar interior, we follow an analogous procedure by beginning with the equation for hydromagnetic equilibrium,

$$\frac{\nabla P}{\rho} + \nabla\varphi = \frac{(\nabla \times \boldsymbol{B}) \times \boldsymbol{B}}{4\pi\rho} = \frac{\boldsymbol{L}}{4\pi\rho} \,, \tag{4.1}$$

where we have familiar expressions for P the stellar pressure, ρ the mass density, and φ the gravitational potential, as well as new variables such as $\boldsymbol{B}$ the magnetic field and $\boldsymbol{L}$ the Lorentz force [1]. The expression $(\nabla \times \boldsymbol{B}) \times \boldsymbol{B} = \boldsymbol{L}$ defining the Lorentz force becomes clear given necessary conditions for hydromagnetic equilibrium; primarily, we require static fields such that the Maxwell-Ampere law reduces to Ampere's law. Then,

$$(\nabla \times \boldsymbol{B}) = \mu_0 \boldsymbol{J} \,, \tag{4.2}$$

such that

$$(\nabla \times \boldsymbol{B}) \times \boldsymbol{B} = \mu_0 \boldsymbol{J} \times \boldsymbol{B} = \rho_q \boldsymbol{v} \times \boldsymbol{B} \,, \tag{4.3}$$

where ρ_q is free charge density and $\boldsymbol{v}$ is charge velocity. Furthermore, the requirement of static fields qualitatively means equation (4.1) arises from a stellar interior where the condition of no internal motion or rotation is assumed [22].

The gravitational potential, conforming to Poisson's equation, is the restated expression (3.20),

$$\nabla^2\varphi = 4\pi G\rho \,, \tag{4.4}$$

such that the functional form for φ as determined in §**3.3** remains consistent in solving for magnetic field configurations. Furthermore, the magnetic field must adhere to Maxwell's equations, such that the field preserves the divergence-free condition,

$$\nabla \cdot \boldsymbol{B} = 0 \,. \tag{4.5}$$

4.2 Magnetic Field Solutions for Barotropic Equations of State

Notice that the left-hand side of (4.1) is entirely composed of gradients of scalar functions. Using the identity, $\nabla \times (\nabla \boldsymbol{A}) = 0$, for $\boldsymbol{A}$ any scalar-valued function, we arrive at an additional constraint for the magnetic field,

$$\nabla \times \left[\frac{\boldsymbol{B} \times (\nabla \times \boldsymbol{B})}{\rho} \right] = 0 \,. \tag{4.6}$$

This expression requires that for a barotropic equation of state of the form, $\rho = \rho(P)$, the magnetic field configuration is constrained by the density. For our model, we determine such an expression via the inverse of equation (3.6b), leading to

$$\rho(P) = \sqrt{\frac{P}{K}} \,. \tag{4.7}$$

Following a procedure detailed by [1] and [22], structural expressions are determined first for the stellar interior without the presence of a magnetic field. Our discussion in Chapter 3 provides us with necessary structural expressions for the $n = 1$ polytrope. Subsequently, equation (4.6) is used to determine an expression for the magnetic field, $\boldsymbol{B}$. In a final step, [1] and [22] use the resulting magnetic field equation to solve for first perturbative order expressions of ρ, P, and φ. In doing so, the authors determine the degree to which the magnetic field, $\boldsymbol{B}$, changes the stellar structure, from which a measure of stellar ellipticity, ϵ, can be determined. By alternative means discussed in §**2.7**, we calculate ellipticity through computational simulation of magnetic-field induced stellar deformation.

4.3 Field Structure

In §**1.2.1**, we discussed the pulsar model which describes the physical structure and external magnetic field necessary to produce strong and focused radio beams aligned along the magnetic axis of the pulsar. These radio beams are the result of charged particles that are excited near the magnetic axis, producing dipole radiation. The production of focused radio beams requires a strong dipolar magnetic field. In particular, equation (1.13) quantifies the strength of the magnetic dipole field near the surface of the star. This condition sets a restriction on potential field configurations which replicate magnetar composition, as the pulsar model requires that these stars must possess strong dipolar fields. Dipole fields are broadly referred to as *poloidal fields*, as their configurations involve field lines directed from pole to pole of the magnetic axis. We now turn to the issue of allowable field configurations for which the field remains in dynamic stability, and unallowable configurations which rapidly evolve and alter the stellar field structure.

4.3.1 Unstable Field Configurations

The hydromagnetic equilibrium conditions outlined in §**4.1** only permit a finite number of solutions for allowable magnetic field configurations in the stellar interior. Certain fields are strictly prohibited by these conditions, leading to unstable field configurations with dramatic time evolution. Flowers and Ruderman (1977) discuss the inherent instability of pure-poloidal stellar magnetic fields with uniform, unclosed field lines in the stellar interior matching an external dipolar field [23]. Figure 4.1 displays such a field configuration with parallel field lines running longitudinally through the star.

To illustrate why such a field is unstable, an analogy can be made between stellar poloidal field configurations and an pair of vertical bar magnets with respective poles aligned side-by-side. As shown in Figure 4.2, when the bar magnets are brought close together, the proximity of like poles causes the bars to rotate until the north pole of one magnet aligns parallel to the south pole of the other. This process reduces the magnetic field energy external to the bar magnets while preserving

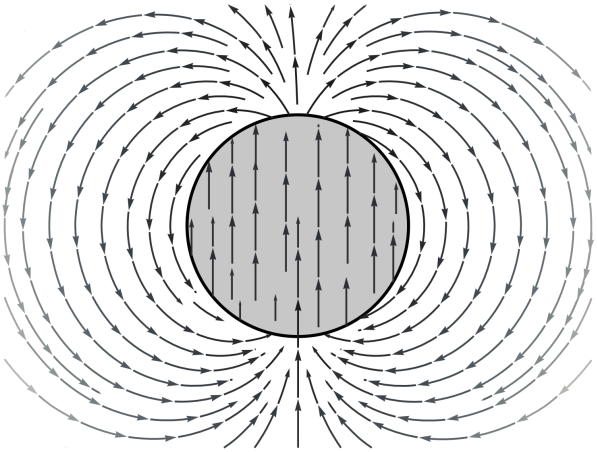

FIGURE 4.1: An unstable purely poloidal magnetic field configuration with unclosed field lines in the stellar interior. The field is uniform throughout the interior and matches to a dipolar field on the exterior.

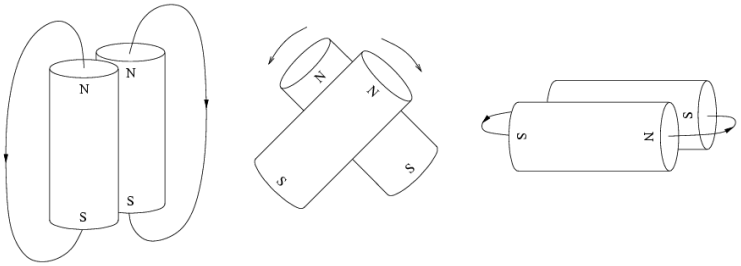

FIGURE 4.2: A bar magnet model illustrating the instability of purely-poloidal magnetic field configurations. The bar magnets rotate to decrease the energy of the external field configuration while preserving the magnetic field energy interior to the bar magnets [24].

their internal field energy. An similar process of field reconfiguration must also occur in purely poloidal fields, reducing the magnetic energy of the field exterior to the star while preserving the energy configuration in the stellar interior.

4.3.2 Stable Field Configurations

Although a purely poloidal magnetic field is an unstable configuration on its own, the field may be stabilized in a number of ways. In newly formed neutron stars, the crustal region undergoes dramatic cooling, resulting in the crystallizing of crustal material [23]. If the time scale over which the magnetic field undergoes reconfiguration, the Alfvén crossing time,

$$t_A = \frac{\sqrt{4\pi\rho}R}{B} \,, \tag{4.8}$$

is greater than the time scale of crustal formation and crystallization, the field does not have sufficient time to evolve before the crust develops. This results in the magnetic field lines becoming "frozen in" near the crust, thus stabilizing the field. [24] show that for a typical magnetar configuration with magnetic field strength in the interior exceeding 10^{15} gauss, $t_A \approx 0.1$ s, whereas crustal crystallization requires ~ 100 s. As a consequence, this process alone can not account for the complete stabilization of a purely poloidal stellar magnetic field.

[23] show that a dipolar field can be stabilized by a toroidal component field which wraps horizontally around the poloidal field. The toroidal field is purely azimuthal, and in the context of spherical coordinates (r, θ, ϕ), can be referred to exclusively by the field component B_ϕ for $\boldsymbol{B} = \{B_r, B_\theta, B_\phi\}$, a vector-valued expression for the stellar magnetic field. Again, authors Flowers and Ruderman provide a useful analogy via the bar magnet model. Figure 4.3 displays a field configuration in which a toroidal field wraps horizontally around both bar magnets, restraining the poloidal field. The currents responsible for producing the toroidal field flow along poloidal field

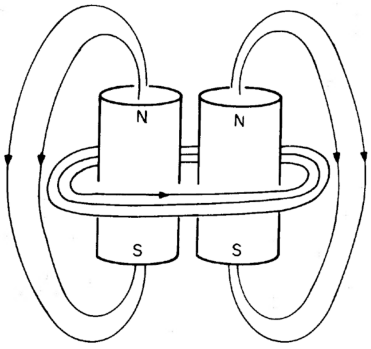

FIGURE 4.3: A purely poloidal field running north to south in the parallel bar magnets can be stabilized by a purely-azimuthal toroidal field wrapping horizontally around the magnets [23].

lines and surround currents which produce the poloidal field. The stability of this configuration depends on the co-dependence of one field component to the other; if, say, the poloidal field begins to alter its configuration and field strength, the toroidal component strengthens, thereby counteracting field instabilities. We refer to field configurations involving both poloidal and toroidal components as *mixed magnetic fields*.

The interdependence between poloidal and toroidal components in mixed field configurations is

further developed in mathematical formalism by [22] and [1]. [22] introduces the field line function $S(r, \theta)$, which takes the form of a constant along poloidal field lines. Similarly, an equation $\beta(S)$ is constant along toroidal field lines. Recalling equations (4.1) and (4.3), the toroidal field B_ϕ can not exert a force, as there exists no structural or magnetic component to oppose the force. Therefore,

$$[\boldsymbol{B} \times (\nabla \times \boldsymbol{B})]_\phi = 0 \, . \tag{4.9}$$

We define field components B_r and B_θ as

$$B_r = \frac{1}{r^2 \sin\theta} \frac{\partial S}{\partial \theta} \, , \tag{4.10}$$

and

$$B_\theta = -\frac{1}{r \sin\theta} \frac{\partial S}{\partial r} \, , \tag{4.11}$$

such that equation (4.9) becomes

$$\boldsymbol{B}_p \cdot \nabla (r \sin\theta \boldsymbol{B}_t) = 0 \, , \tag{4.12}$$

where the poloidal field is expressed as $\boldsymbol{B}_p = \{B_r, B_\theta\}$ and the toroidal field as $\boldsymbol{B}_t = B_\phi$. Then, via equation (4.12), we find that

$$B_\phi = \frac{\beta(S)}{r \sin\theta} \, , \tag{4.13}$$

such that β is a function of S, and importantly, we find that the toroidal field, B_ϕ, is a function of the poloidal component in mixed magnetic field configurations.

4.4 Mixed Field Solutions for the N = 1 Polytrope

4.4.1 Eigenvalue Solutions

In determining mixed field solutions for the $n = 1$ polytrope via the density constraint equation (4.6), solutions arise for which the eigenvalue λ is related to the functions β and S by

$$\beta = \frac{\pi \lambda}{R} S \, , \tag{4.14}$$

where S is of the form $S(r,\theta) = A(r)\sin^2\theta$ and $A(r)$ is a function which completely determines the radial dependence of the field line function, $S(r,\theta)$ [1][22]. Haskell et al. (2008) determine values for λ as arising from roots to the transcendental equation

$$\pi\lambda(\lambda^2-1)\cos\pi\lambda - (3\lambda^2-1)\sin\pi\lambda = 0\ . \tag{4.15}$$

In Table (4.1) below, we list the first few eigenvalue solutions λ_n to equation (4.15), as well as a number of solutions for $n \gg 1$. We find that in the case of $n \gg 1$, eigenvalue solutions approach the form $\lambda_n = n + 3/2$.

λ_n	Numerical Value
λ_1	2.3619
λ_2	3.4079
λ_3	4.4301
...	...
λ_{99}	100.497
λ_{100}	101.497
...	...
λ_{500}	501.499

TABLE 4.1: Eigenvalues determining allowed relative strengths for the toroidal component of the mixed magnetic field equations. The first few eigenvalues are shown, followed by results for $n \gg 1$ to illustrate the approximate relationship $\lambda_n = n + 3/2$ for sufficiently large n.

4.4.2 Field Expressions

Haskell et al. (2008) find that for the $n = 1$ polytrope and for eigenvalues λ, solutions to the mixed magnetic field configuration take the form

$$\boldsymbol{B} = \left\{\frac{2A\cos\theta}{r^2}, \frac{-A'\sin\theta}{r}, \frac{\pi\lambda A\sin\theta}{rR}\right\}\ , \tag{4.16}$$

and where A is

$$A = \frac{B_k R^2}{(\lambda^2-1)^2 y}\left[2\pi\frac{\lambda y\cos(\lambda y) - \sin(\lambda y)}{\pi\lambda\cos(\pi\lambda) - \sin(\pi\lambda)} + \Big((1-\lambda^2)y^2 - 2\Big)\sin(y) + 2y\cos(y)\right]\ . \tag{4.17}$$

The constant B_k sets the strength of the magnetic field. The field strength at the stellar surface, which we label B_s, imposes a constraint on the value of B_k, as we wish for the value of B_s to adhere to magnetar surface field strengths of order 10^{15} G. We experimentally determine for our simulation that a value of $B_k = 1 \times 10^{17}$ G results in a surface field strength of approximately $B_s \approx 2.5 \times 10^{15}$ G. This designation is consistent with the notion that internal magnetic field strengths can range up to a few orders of magnitude higher than surface fields [3].

For our field expressions, the parameter y has been implemented to simply equation (4.17) where

$$y = \frac{\pi r}{R} \, . \tag{4.18}$$

In Figure (4.4), we generate scalar plots of $|\boldsymbol{B}|$ for various values of λ in the xz-plane. Notice that as the value of λ increases, the relative strength of the toroidal field increases, meaning the eigenvalue λ parameterizes the strength of the toroidal component with respect to the poloidal field. Haskell et al. (2008) use first perturbative order to solve for perturbations in the stellar structure, and find that for λ_n where n for a mixed field configuration, the star becomes increasingly prolate [1].

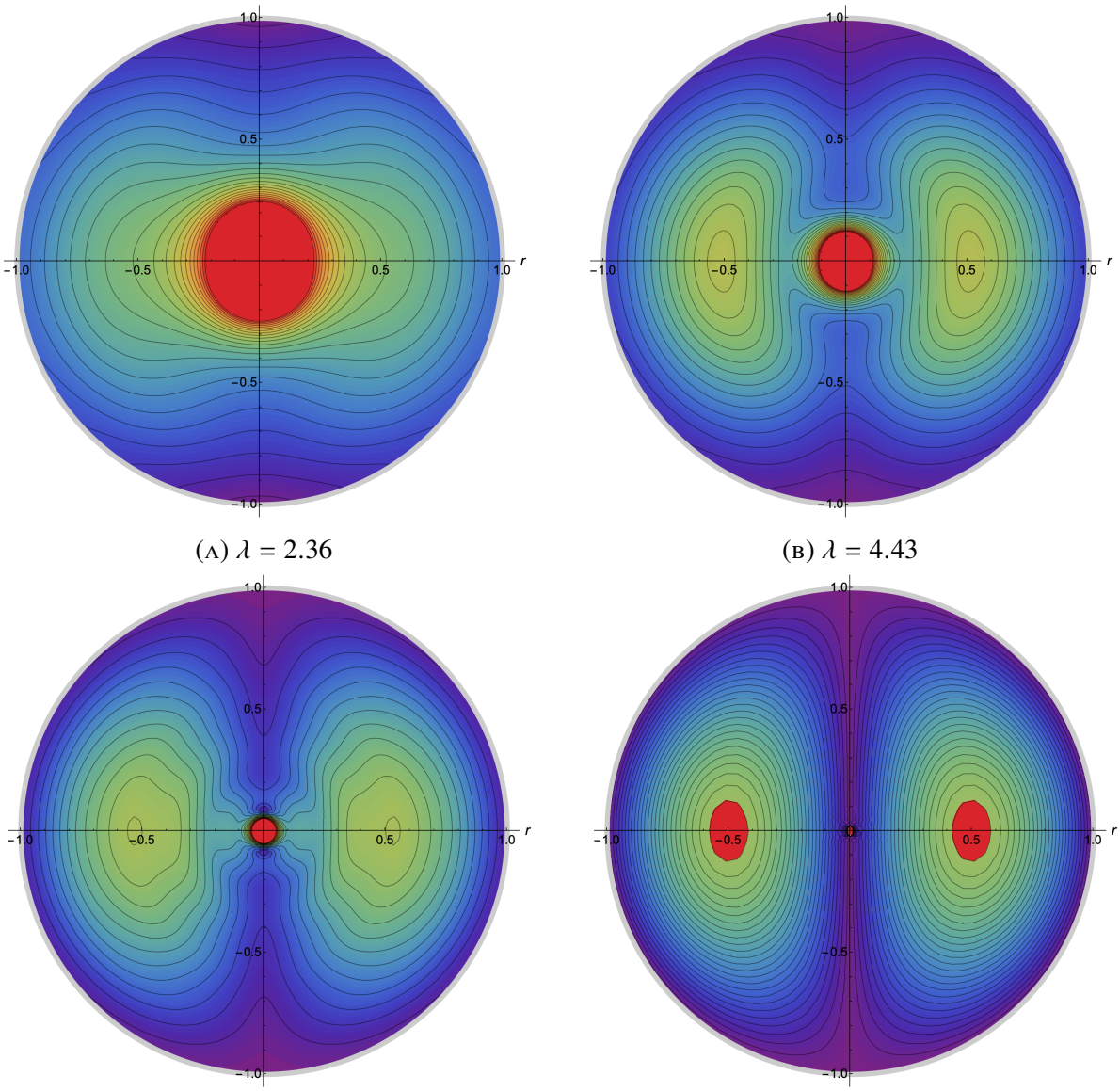

(A) $\lambda = 2.36$

(B) $\lambda = 4.43$

(C) $\lambda = 9.467$

(D) $\lambda = 100.5$

FIGURE 4.4: Contour plots of internal magnetic field magnitude against normalized radius ($r = 1.0 = R$) for mixed-field configurations. As the parameter λ increases, the toroidal component of the mixed field increases in relative magnitude to the poloidal component.

CHAPTER 5

NUMERICAL METHODS

5.1 The Magnetohydrodynamic Equations

In Chapters 3 and 4 we develop expressions for the structural composition and magnetic field configuration which satisfy requirements of hydrostatic and hydromagnetic equilibrium, respectively. These conditions jointly determine stability of fluid comprising the stellar structure in the presence of a magnetic field. However, as we note in §**4.2**, subsequent introduction of a magnetic field model following the determination of stellar structure equations introduces minute perturbations to structural variables such as pressure and density. Whereas Haskell et al. (2008) determine these perturbations via first-order perturbation theory, we implement computational methods in evolving the initial model configuration to determine the perturbed equilibrium configuration [1]. Subsequent analysis of the evolved simulation informs estimate of continuous gravitational wave strain, h, as a result of stellar deformation quantified by the ellipticity, ϵ.

Although the expressions for hydrostatic and hydromagnetic equilibrium allow determination of structural and magnetic field equations which are stable, these solutions possess no explicit time dependence. Therefore, we require a set of equations governing the time-dependent evolution of both the stellar structure and magnetic field. The *magnetohydrodynamic (MHD)* equations provide the necessary set of conditions to evolve our stellar model, imposing both time-independent constraints and the conservation of time-dependent quantities.

In Chapter 3, we construct a stellar structure model, implementing an $n = 1$ polytropic EOS under various considerations, the foremost being the equation's utility in accurately modeling neutron star structure while providing a straightforward, analytic expression. Although this choice of EOS does come with trade-offs as we discuss in Chapter 7, we apply a similar philosophy of balancing utility with ease of implementation in our choice of *ideal* MHD equations. A set of assumptions are adopted for ideal MHD physics which simplify its form, including omission of

effects due to resistivity and thermal diffusion, both physical phenomenon which are mitigated by attributes of the neutron star stellar interior including superconductivity and nearly isothermal composition. Under these considerations, the ideal MHD equations provide a useful basis for evolving our stellar model while offering accessible utilization in numerical methods. Below, we list the principle equations of ideal magnetohydrodynamics:

$$\frac{\partial \rho}{\partial t} + \nabla \cdot (\rho \mathbf{v}) = 0 \,, \tag{5.1a}$$

$$\rho \left(\frac{\partial}{\partial t} + \mathbf{v} \cdot \nabla \right) \mathbf{v} + \nabla p - \frac{1}{\mu_0} (\nabla \times \boldsymbol{B} \times \boldsymbol{B}) = 0 \,, \tag{5.1b}$$

$$\frac{\partial p}{\partial t} + \mathbf{v} \cdot \nabla p + \gamma p \nabla \cdot \mathbf{v} = 0 \,, \tag{5.1c}$$

$$\frac{\partial \boldsymbol{B}}{\partial t} + \nabla \times (c\boldsymbol{E}) = 0 \,, \qquad \nabla \cdot \boldsymbol{B} = 0 \,. \tag{5.1d}$$

Equation (5.1a) is the mass continuity equation, expressing conservation of mass given there exist no flow source or sink terms in our computational domain. Equation (5.1b) is the Cauchy momentum equation regarding momentum transport. Equation (5.1c) expresses conservation of entropy, modeling an adiabatic fluid. The final component, Equation (5.1d), is Faraday's law, were crucially, the divergence constraint is specified for the magnetic field [25]. These non-linear partial differential equations must be solved via finite-difference numerical methods, forming the next topic of discussion.

5.2 Numerical Solver: The PLUTO Code

5.2.1 The Computational Domain

In order to initialize and evolve our simulation under our chosen set of stellar structure and magnetic field equations, we implement `PLUTO`, a freely-distributed C-based code intended for simulation of astrophysical phenomena involving fluid dynamics. `PLUTO` is readily applicable to numerous physical circumstances, including simulation of fluid configurations which evolve in accordance with the ideal MHD equations. `PLUTO` allows the user to specify a computational domain in which simulation variables such as density, pressure, and the magnetic field components are specified over

a finite mesh grid. We implement a spherically symmetric computational domain in accordance with the spherical symmetry present in our equations for stellar structure and the magnetic field. Below, Figure 5.1 displays a single hemisphere of the computational domain. One can clearly note a difference in relative grid resolution throughout the domain. Specifically, we set a higher radial grid cell resolution of 50 cells from $r = 0$ to $r = 1.0 = R$, where the dimensions of our domain are specified in units of normalized radius r/R. We discuss further the choice of separate radial grid resolution interior and exterior to the star in §**6.2.1**. We utilize lower radial mesh resolution exterior to the star, with 2 grid cells radially spanning $r = 1.0$ and $r = 1.1$. For $0 < \theta < \pi$, referred to as the polar angle from the north to south pole, 30 grid cells are specified. The azimuthal angle, for $0 < \phi < 2\pi$, is set to a resolution of 60 grid cells, or 30 cells per hemisphere.

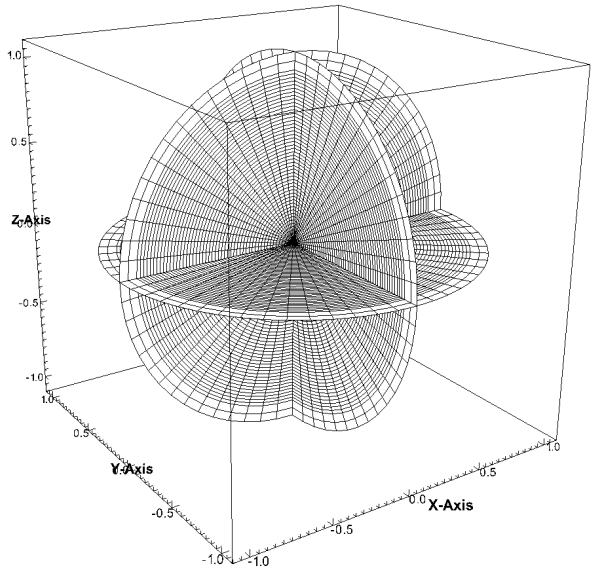

FIGURE 5.1: A three-slice cutaway of the computational domain. Notice the regional variation in grid resolution.

5.2.2 Finite Difference Methods

The discretization of the computational domain into hundreds of finite-volume grid cells necessitates numerical methods for solving the ideal MHD equations based on finite-difference schemes. To provide motivation for the use of discrete methods, we discuss numerical methods for discretely

approximating an ordinary derivative. Recall the definition of an ordinary derivative is

$$\frac{df}{dx} = \lim_{h \to 0} \frac{f(x+h) - f(x)}{h} \,, \tag{5.2}$$

such that the discretization h infinitesimally approaches zero, allowing analytic interpretation of df/dx. While this definition allows *exact* evaluation of analytic expressions for derivatives, computational methods require the use of non-zero discretization, as infinitesimal limits have no numerical equivalent. Thus, numerical *approximation* of derivatives, as well as anti-derivatives, require finite-difference methods for evaluation. Extending our example of approximating an ordinary derivative for a continuous and differentiable function, $f(x)$, by numerical methods, the *central-difference scheme* approximates df/dx as

$$\frac{df}{dx} = \frac{f(x+h) - f(x-h)}{2h} + \mathcal{O}(h^2) \,. \tag{5.3}$$

We note that for sufficiently small discretization of h, say, $h \sim 10^{-8}$, we may indeed numerically approximate df/dx to near machine accuracy, $\epsilon_{machine} \sim 10^{-16}$. Although the central-difference scheme is simply one example of numerical methods employed for approximating derivatives, the approximation of analytic expressions including the definition of the derivative (equation (5.2)) by the central difference scheme (equation (5.3)) highlights a principle of approximating analytic expressions such as derivatives and anti-derivatives which rely on infinitesimal discretization. That is, finite difference methods are *required* for the computational implementation of derivatives and anti-derivatives, and we must choose numerical schemes which minimize the error between analytic evaluation and finite-difference approximation for a function [26].

Under these considerations, `PLUTO` provides the user with various numerical algorithms which solve the ideal MHD equations via finite difference methods, thus evolving an initial configuration in accordance with the conditions specified by equations (5.1a) through (5.1d). Specifically, a chosen solver iteratively determines the change in grid-cell variables such as the density, pressure, and magnetic field based on surrounding grid-cell quantities for respective variables. Qualitatively, this means the chosen solver must determine the evolution of these grid-cell variables by interpolation, evaluating the flux, or change in a variable quantity for a specified grid-cell, by utilizing the

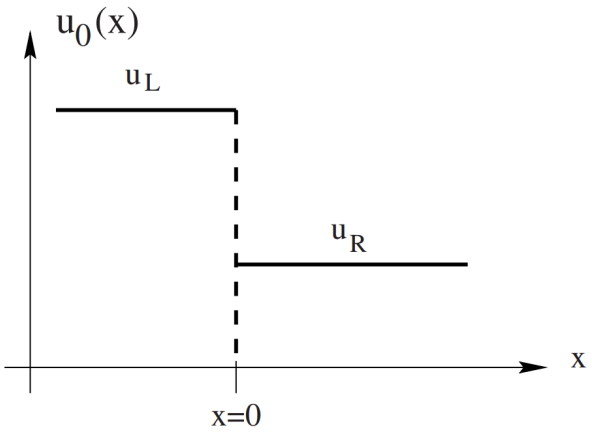

FIGURE 5.2: Schematic for initial data characterizing a one-dimensional Riemann problem [27]. In our model, to the left of $x = 0$ represents the value (u_L) for a cell variable, say density, and $x > 0$ represents an adjacent grid cell with a different variable value U_R. The role of the solver is the determine how the adjacent grid-cell values change over a time dt, based on the flux of surrounding grid-cell quantities for the specified variable .

variable's flux in surrounding grid-cells. This process is not unlike the central-difference scheme, which determines df/dx by implementing the surrounding values $f(x+h)$ and $f(x-h)$. Numerical solvers which use finite-difference methods to solve systems which evolve via continuity equations of the form $\partial_t f + \mathbf{v}\partial_x f = 0$ are known as *Riemann solvers*. These solvers determine solutions to a Riemann problem, which consists of determining how constant piecewise data across a boundary evolves in time. For our simulation, there exists a Riemann problem for each grid-cell boundary, as the discretization of the computational domain requires finite-differences between adjacent grid cell quantities for a particular variable. As with the numerical approximation of ordinary derivatives, many computational schemes exist for solving Riemann problems, and `PLUTO` provides the user with a variety of Riemann solvers from which to choose. In selecting a Riemann solver, one must weigh considerations for numerical accuracy and computational efficiency, a common theme in our methodology. We implement the Hartman, Lax, Van Leer or `hllc` Riemann solver, which provides a balance of accuracy and efficiency.

5.3 Data Visualization: VisIt

Once PLUTO has generated solutions to the ideal MHD equations for our model by implementing the `hllc` Riemann solver, data are written to files after the simulation has evolved for a discrete simulation time step of 1×10^{-3} s. We require the use a visualization tool for graphically displaying these computational data. We utilize `VisIt`, a freely-distributed, open-source visualization utility devloped by Lawrence Livermore National Laboratory, which allows data analysis via 3-D rendering of scalar and vector fields. We implement `VisIt` for generating detailed visualizations of both structural and magnetic field evolution.

CHAPTER 6

RESULTS

6.1 Computational Requirements

6.1.1 Dimensionless Units

Throughout this thesis, we utilize c.g.s. units for physical quantities, as this unit basis is a widely adopted convention in the field of computational astrophysics. However, given the scale of quantities we wish to employ, e.g. stellar mass $\sim 10^{33}$ g, magnetic field magnitude $\sim 10^{15}$ G, and stellar radius $\sim 10^{6}$ cm, we must anticipate potential hazards in direct computation of numerical solutions as a result of extremely large or small input quantities. In particular, such implementation may result in an *ill-conditioned* system, where small changes in input can result in dramatic changes in the solution [26].

Fortunately, we can avoid ill-conditioned solutions by posing the set of initial conditions in an alternative unit basis. Therefore, we adopt non-dimensional units, for which `PLUTO` allows ready implementation via a set of unit bases. `PLUTO` allows the user to specify unit bases for density, length, and velocity. Once a quantity is calculated in c.g.s. units, it is subsequently divided by the appropriate combination of unit bases which render the value dimensionless. Consider the example of pressure p, which has c.g.s. units of $\mathrm{g{\cdot}cm^{-1}{\cdot}s^{-2}}$. The appropriate combination of unit bases which provide the proper dimensionless transformation is

$$p = \frac{p_{cgs}}{\rho_0 v_0^2} \,, \tag{6.1}$$

where p is the dimensionless expression for pressure, and p_{cgs} is the value of the pressure in c.g.s. units. The unit bases p_0 and v_0 for density and velocity, respectively, are freely specified by the user to fit the simulation requirements.

Table 6.1 lists unit bases and corresponding magnitudes we utilize for our computational simulation. The magnitude of each unit basis is chosen with consideration to minimizing the

magnitude of important simulation quantities, such as the magnetic field, for which a magnitude of $\sim 10^{15}$ G can be reduced to $\sim 10^{1}$ in dimensionless units.

Unit Basis	c.g.s. Value
ρ_0	1×10^8 g·cm^{-3}
l_0	1×10^{10} cm
v_0	1×10^{10} cm· s^{-1}

TABLE 6.1: Unit bases utilized in this thesis. Values were chosen with the intent of minimizing the magnitude of dimensionless expressions for pressure, gravitational potential, magnetic field strength, etc.

In general, the computational procedure from initial conditions to final solution utilizes dimensionless conversions in the following way:

a) Calculate numerical value in c.g.s.

b) Convert to dimensionless quantity via appropriate combination of unit bases.

c) Evolve simulation via `hllc` numerical solver. Determine solution for quantity.

d) Convert value back to c.g.s.

e) Write data to file.

6.2 Validation of Model Stability

In this section, we verify that both our chosen structural model and magnetic field configuration are dynamically stable by evolving each in time to evaluate whether large-scale structural instabilities form.

6.2.1 Hydrostatic Equilibrium

In order to test that our stellar model is in hydrostatic equilibrium, balancing gravity with the change in pressure, we generate a stellar simulation where $|\boldsymbol{B}| = 0$, effectively turning off the magnetic field. Our analysis focuses principally on the density and its evolution under such simulation. Because the pressure is related to the density by equation (3.6b), we immediately have an indication

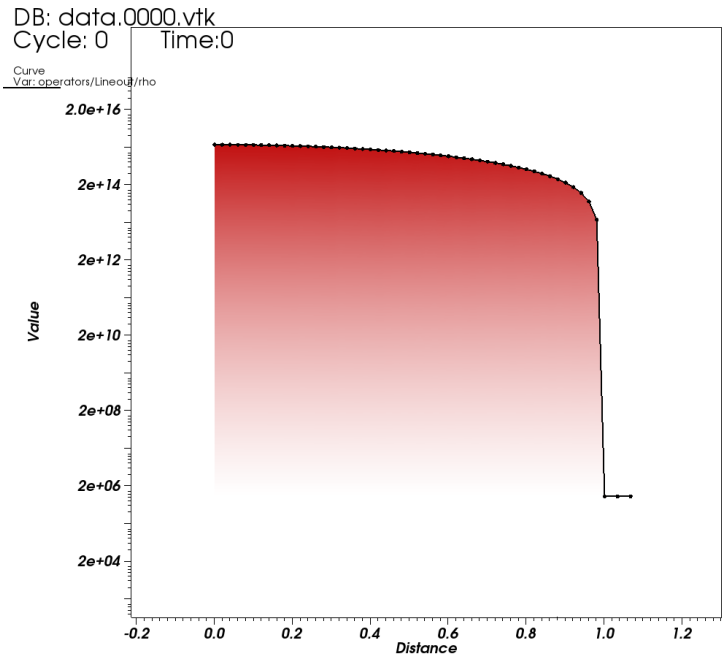

FIGURE 6.1: Semi-log plot for the stellar density profile at simulation time t = 0 s. Density in g·cm^{-3} is plotted against normalized stellar radius.

of the pressure profile evolution given the degree of change in the density. Thus, indication of little change in the density profile under the conditions of hydrostatic equilibrium indicates correspondingly slight change in pressure throughout the star, and in turn, verification of structural stability.

Figure 6.1 displays a semi-log plot of the initial configuration of the stellar density profile, obtained by plotting density values along the x-axis of the computational domain where the star is centered at the origin. The choice of the x-axis is arbitrary, as the star possesses spherical symmetry. Each point along the pressure profile indicates a grid cell within the computational domain. It is valuable to note the large-scale difference between adjacent density values immediately interior to the star and at the stellar surface. The difference is approximately seven orders of magnitude, which poses potential issues in numerical simulation across this boundary. Recall that evolution of the computational model requires solving many Riemann boundary problems between finite differences in adjacent grid cell volumes. Due to the dramatic scale of the finite-difference problem for density near the stellar boundary, we expect computational artifacts in the form of diffusion,

or excessive density flux, as a result of the inherent limitation of the discretized simulation at large-scale boundary problems. The impact of such diffusion can be mitigated by increasing radial resolution, thus lowering the finite difference between adjacent grid cells. Indeed, this forms the motivation for our choice of higher radial grid cell resolution interior to the star. Even higher radial grid cell resolution would function to further mitigate diffusion near the stellar boundary; however, consideration must be made for balancing computational accuracy and efficiency, and with increased grid cell resolution comes the cost of compute time. We further discuss the impact of resolution on compute time in Chapter 7. Due to these considerations and computational limitations, we adopt a middle ground between exceedingly time-intensive, high-resolution simulations and lower resolution studies, with the acknowledgement that some computational artifacts in the form of diffusion may inherently develop through evolving our stellar model.

Figure 6.2 displays results from hydrostatic equilibrium tests with the magnetic field removed from the simulation in order to exclusively measure structural stability. To evaluate the change in density over the course of the simulation, we analyze the time derivative of density, $d\rho/dt$, at various timesteps of the computational simulation. The left column is comprised of pseduocolor plots at three chosen simulation timesteps allowing visualization for the value of $d\rho/dt$ across the xz-plane of the computational domain. The blue horizontal line running through the x-axis of each pseudocolor plot corresponds to a line of data sampled to create the second column of accompanying line plots. These plots are evenly symmetric, and again, the choice of line plots along the x-axis is arbitrary given the stellar spherical symmetry.

At $t = 0$ corresponding to the initial conditions for the simulation, we trivially observe no change in density. However, as our prior discussion of computational diffusion anticipates, in the first iteration of simulation evolution at $t \approx 0.001$ s, we observe abrupt changes in density along grid cells adjacent to the stellar boundary. Line plot (D) clearly displays this phenomenon, as density is rapidly evacuated from a spherical shell of grid-cell centered density values from $r = 0.97$ to $r = 0.99$, where the radial depth of each grid cell is 0.02 units of normalized radius such that these grid cells represent the outer-most layers of the stellar interior. We notice a similar phenomenon

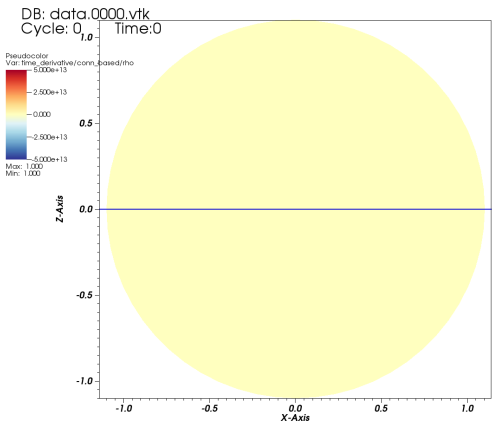

(A) x–z plot: $d\rho/dt$ at t = 0 s

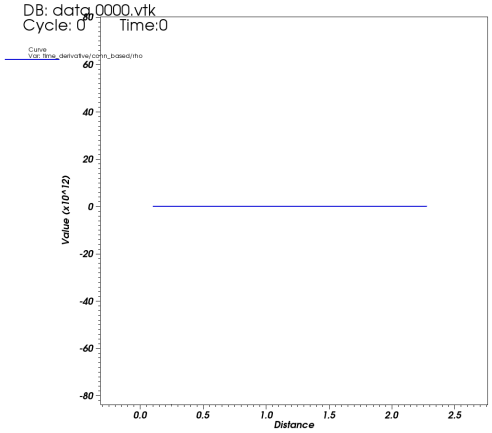

(B) x-axis line plot: $d\rho/dt$ at t = 0 s

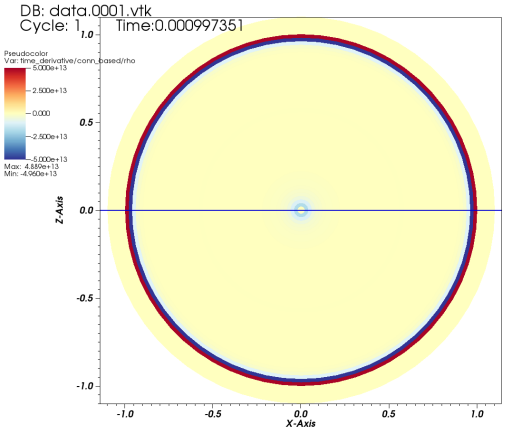

(C) x–z plot: $d\rho/dt$ at t $\approx 0.001s$

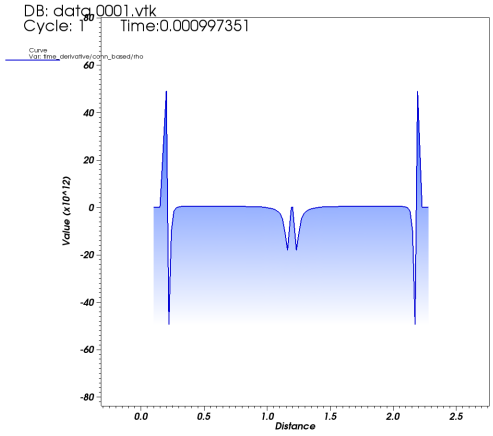

(D) x-axis line plot: $d\rho/dt$ at t $\approx 0.001s$

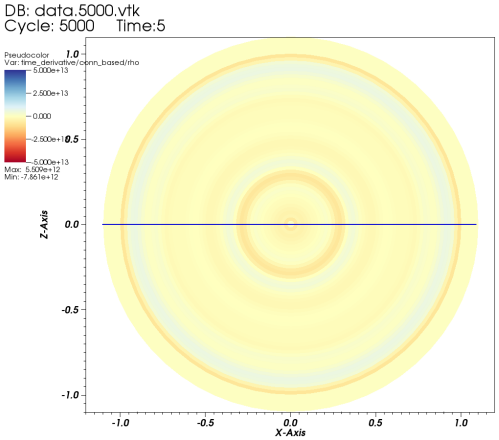

(E) x–z plot: $d\rho/dt$ at t = 5.0 s

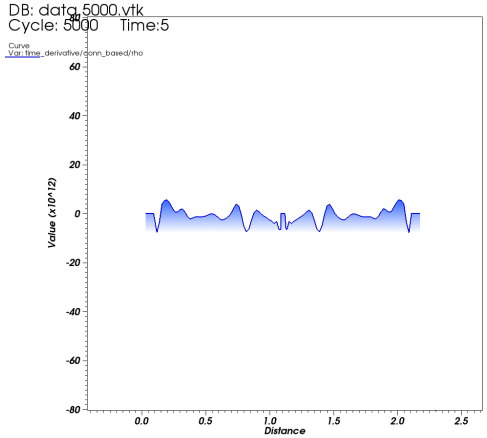

(F) x-axis line plot: $d\rho/dt$ at t = 5.0 s

FIGURE 6.2: Graphical depictions for $d\rho/dt$ at computation times $t = 0$, $t \approx 0.001$, and $t = 5.0$ s. The left column (plots (A), (C), and (E)) displays pseudocolor plots for the value of $d\rho/dt$ in the xz-plane. The blue horizontal line running through each pseudocolor plot corresponds to the line plot data of plots (B), (D), and (F) in the right column.

along the interior radial boundary, $r = 0$. Given that the volume of each grid cell is proportional to r^2, the mesh density in this region is much higher than outer radial regions. This may result in an overrefinement of the numerical solution near the core, producing additional non-physical diffusion. This suggests there is likely a balance between excessively high and low mesh resolutions to minimize erroneous diffusivity in these regions. Future investigations may choose to further evaluate methods of minimizing these computational artifacts by adjusting mesh resolution accordingly.

Plots (E) and (F) display $d\rho/dt$ after the simulation has evolved to $t = 5.0$ s in computational time, corresponding to the 5000 iteration of the solution. Notice that initial perturbations present in the $t \approx 0.001$ s solution are significantly diminished after 5000 computational iterations. We notice spherically symmetric perturbations propagating through the stellar interior; however, these artifacts are damped by the stellar medium, and are rapidly attenuated over the course of successive simulation iterations. Therefore, although non-physical artifacts manifest in the first iteration of the simulation (plots (D) and (E)), their effect is significantly diminished under relatively short time scales in computational evolution.

To ensure these computational artifacts have little impact on the large-scale structure of the stellar interior, Figure 6.3 graphs the semi-log density plot at $t = 0$ s from Figure 6.1 beside a

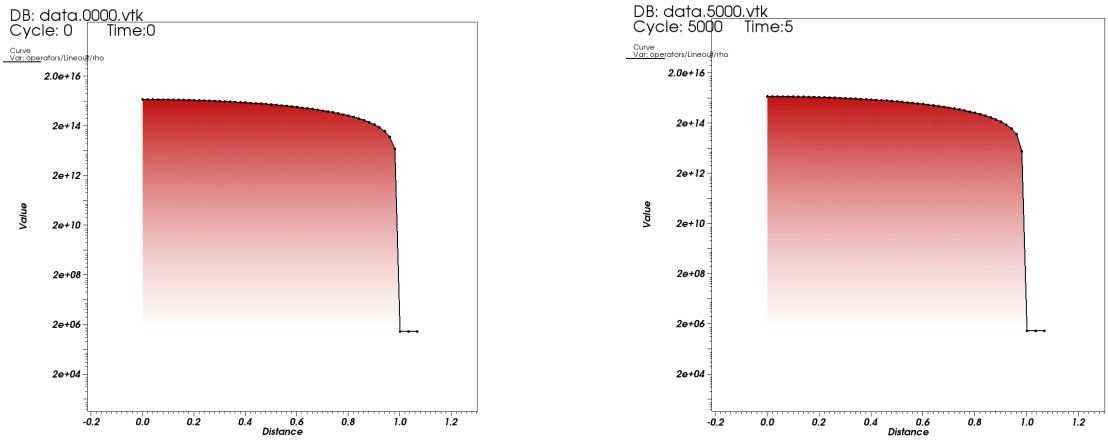

(A) Density profile, t = 0 s

(B) Density profile, t = 5.0 s

FIGURE 6.3: Semi-log plots for the stellar density profile along the x-axis at $t = 0$ (left) and $t = 5.0$ (right).

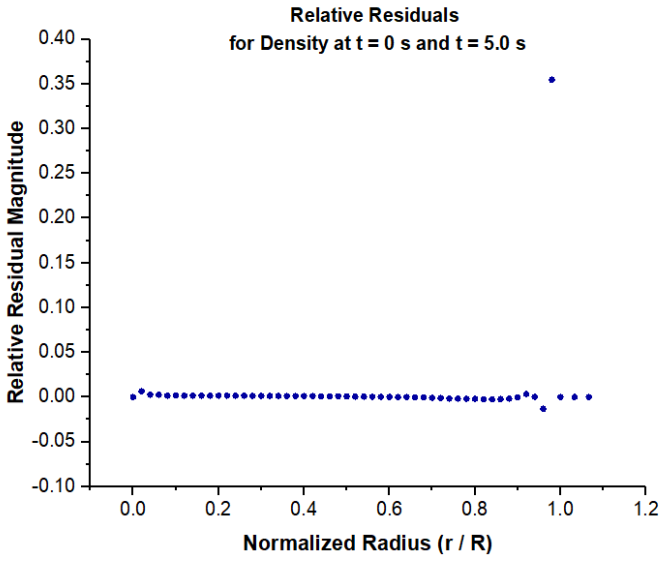

FIGURE 6.4: Relative residual plot comparing the initial configuration of the stellar density profile to the profile after simulation time $t = 5.0$ s.

comparable graph for $t = 5.0$ s. Qualitative comparison between these graphs clearly indicates that the overall density profile predominantly retains its initial structural configuration.

To provide quantitative analysis between these density profiles, we display the relative residuals between Figure 6.3 plots (A) and (B) in Figure 6.4. We define relative residuals in the following way:

$$\Re(i)_{\rho(i)^*,\,\rho(i)} \equiv \frac{\rho(i)^* - \rho(i)}{\rho(i)^*}\,, \tag{6.2}$$

where $\rho(i)^*$ is the value of the density at $t = 0$ for i a discretized radial point along the line plots of Figure 6.3, and $\rho(i)$ is the corresponding density value at $t = 5.0$ s. These relative residuals help us to quantify the difference between the initial structural configuration and after elapsed time of the simulation.

An ideal fit between density profiles at $t = 0$ s and $t = 5.0$ s corresponding to a system at hydrostatic equillibrium would result in a relative residual plot with all residuals equal to zero. With the narrowly localized exception of the residual point corresponding to the radial grid-cell at $r = 0.99$, we find strong consistency with the ideal hydrostatic equilibrium model where all residuals are zero. Indeed, we compute the mean of relative residuals to be 6.98×10^{-3}, providing quantitative support that the condition of hydrostatic equilibrium is met by our model.

6.2.2 Hydromagnetic Equillibrium

Recall our discussion of stable field configurations in §**4.3.2**. We based the stability of a given magnetic field configuration on its ability to evolve under Alfvén time scales, which refer to the time necessary for Alfvén waves to propagate throughout the magnetic field. These waves are induced by tension in the field lines, and determine the geometric evolution of the field configuration [25]. Therefore, we base analysis of the magnetic field configuration on the Alfvén time scale of our magnetic field configuration.

For a homogeneous plasma with uniform density ρ_0 and magnetic field strength $_0$, the velocity of an Alfvén wave is

$$v_A = \frac{B_0}{\sqrt{\mu_0 \rho_0}} \,. \tag{6.3}$$

As density and magnetic field stength vary in our model, we determine a volume averaged value for the Alfvén velocity, $\bar{v}_A$, where $\bar{v}_A \approx 2.736 \times 10^9$ cm·s^{-1}. Equation (4.8) for the Alfvén crossing time can thus be alternatively expressed as

$$t_A = \frac{d}{v_A} \tag{6.4}$$

where d is the wavelength of the Alfvén wave, which in the stellar interior is $\sim R = 10^6$ cm [28]. We compute the volume-averaged Alfvén crossing time for our model to be $\bar{t}_A \approx 0.4$ ms, which is in good agreement with prior evaluation of the Alfvén crossing time for interior magnetic fields in highly magnetic neutron stars [28].

In assessing the stability of our model's magnetic field configuration, the computed Alfvén crossing time indicates that robust analysis of the field's stability may be conducted by analyzing the field configuration after dozens or hundreds of Alfvén crossings, as there are $\sim$ 2700 Alfvén crossings in one second of the simulation. We base analysis of the magnetic field configuration stability by comparing the initial field configuration to the evolved state after 100 Alfvén crossings, corresponding to a simulation time $t \approx 0.037$ s. Despite the relatively short simulation duration, this time scale is appropriate for analysis of field stability given the computed Alfvén crossing time. As an aside, we remark on potential concerns one may raise regarding the simulation time

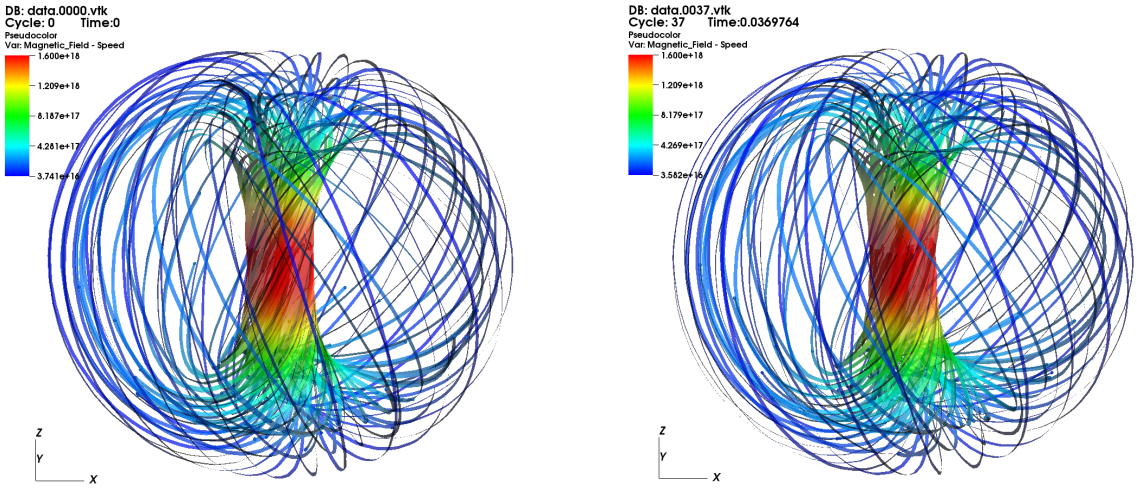

(A) $\bar{t}_A = 0$ (B) $\bar{t}_A = 100$

FIGURE 6.5: Plot (A) displays a streamline plot for initial configuration of the poloidal component field, corresponding to $t_A = 0$. Plot (B) shows the field after 100 Alfvén crossings, confirming that the geometry of the field is preserved. Field lines sweep up through the central z-axis of the star and out through the crustal region, appearing to twist along each path as the toroidal field constrains the pure-poloidal instability. Note that the field is confined to the interior of the star.

step size (1 ms) as potentially too coarse for resolving changes due to Alfvén wave propagation. While data files are generated after the simulation has advanced by 1 ms in simulation time, the time discretization, dt, implemented by the `hllc` numerical solver is of order 10^{-5} s. Thus, the numerical "time resolution" between Alfvén crossings is of order 10^1, such that analysis of the model's field configuration under Alfvén time scales is justified.

Following a similar approach to our analysis of hydrostatic equilibrium, we offer both qualitative and quantitative evidence for supporting the claim that our magnetic field model is structurally and dynamically stable. First, we provide analysis of the magnetic field by presenting qualitative comparisons for both poloidal and toroidal component fields in juxtaposing their respective evolution under 100 Alfvén crossing times. We plot streamlines of each component magnetic field, which are produced by integrating along trajectories of the vector-valued magnetic field. Thus, streamlines provide a method of analyzing the geometry of the field configuration after a specified number of Alfvén crossings. Figure 6.5 displays streamlines of the poloidal component field at both $t_A = 0$ and $t_A = 100$. We notice that the geometry of the field is well preserved, providing initial support

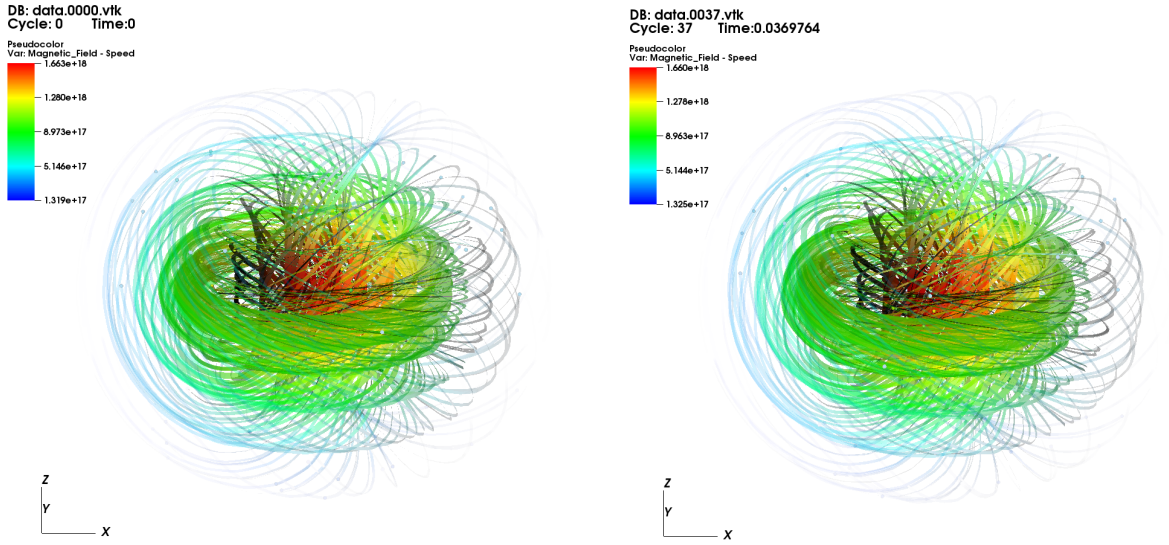

(A) $\bar{t}_A = 0$ (B) $\bar{t}_A = 100$

FIGURE 6.6: Streamline plots highlighting the initial configuration of the toroidal field in green (Plot A) and after 100 Alfvén crossings (Plot B). Opacity of the outer poloidal field lines has been reduced to aid visualization of the inner toroidal component.

for stability of the poloidal component field configuration. Figure 6.6 displays a similar comparison for the toroidal component field. Both figures provide a preliminary conclusion that the large-scale structure of the magnetic field model is maintained through 100 Alfvén crossings, and that the mixed-field model is indeed dynamically stable.

While magnetic field streamline visualizations are derived from the vector-valued field, we also plot the field itself to discern how well the geometry of the vector field is preserved under 100 Alfvén crossings. Figure 6.7 displays visualizations of both the poloidal component vector field (plots (A) and (B)) and the toroidal component field (plots (C) and (D)) for $\bar{t}_A = 0$ and $\bar{t}_A = 100$. These plots highlight how well the configuration of the magnetic field is preserved under 100 Alfvén crossings, and further support the claim that the mixed field configuration we utilize in this thesis adheres to the condition of structural stability.

Additionally, we expect that for a stable magnetic field configuration, the field strength of both the poloidal and toroidal fields should remain nearly constant through Alfvén time scales. This stability condition does not preclude slight variations in component field strength, and indeed, as we note in §**4.3.2**, the condition of dynamic stability for mixed magnetic field requires that slight

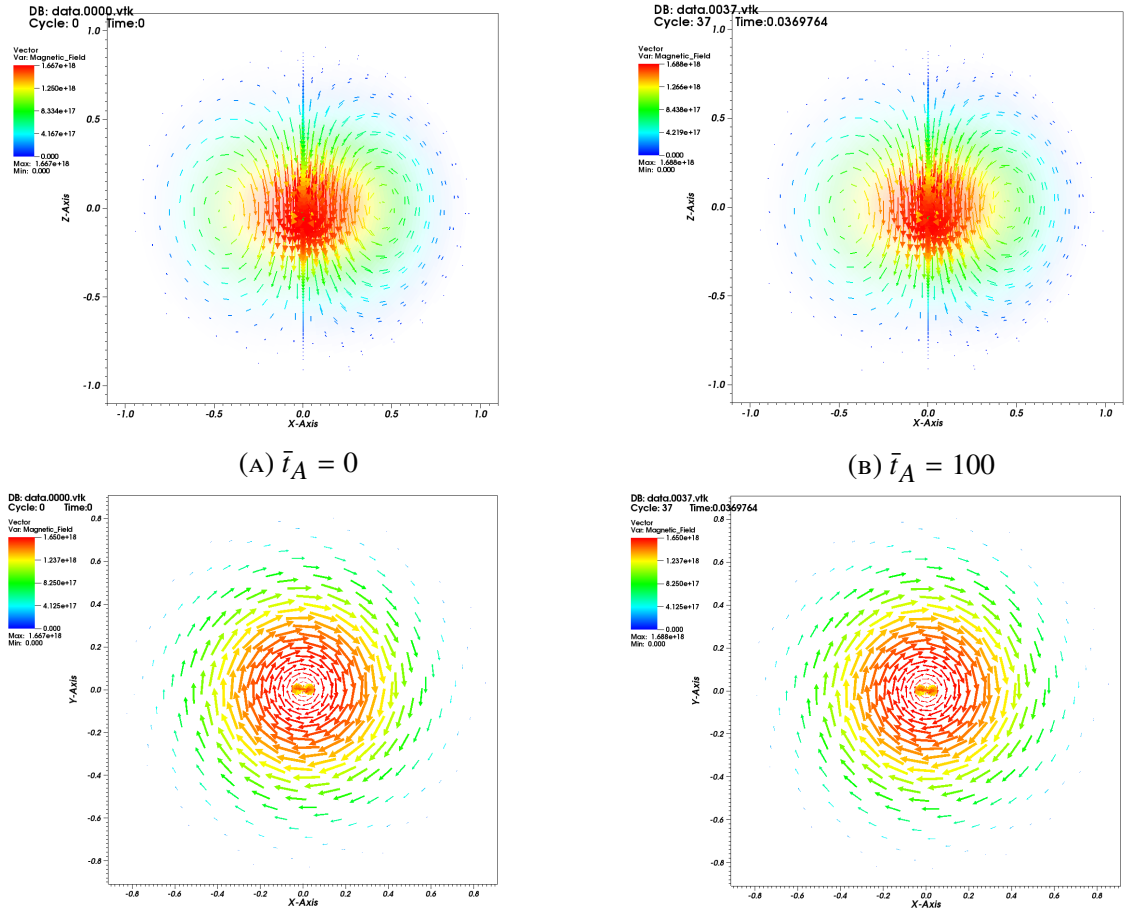

(A) $\bar{t}_A = 0$ (B) $\bar{t}_A = 100$

(C) $\bar{t}_A = 0$ (D) $\bar{t}_A = 100$

FIGURE 6.7: Vector plots for the poloidal and toroidal component field displaying initial configuration and field after 100 Alfvén crossings. The poloidal field is displayed in plots (A) and (B), and the toroidal field is featured in plots (C) and (D).

variation in one component field must counterbalance the change in the other field. However, as the initial conditions for our simulation specify a non-perturbed field solution at hydrostatic equilibrium, we expect to find minimal change in the field configuration over Alfvén time scales. Otherwise, dramatic variations in component field strength would contradict the conclusion of stability for the magnetic field configuration.

In Figure 6.8, we plot the volume-averaged component field magnitude for the poloidal and toroidal fields through 100 Alfvén crossings. Notice that the magnitude of each component field is nearly constant across 100 Alfvén crossings. We analyze these field-magnitude variations more

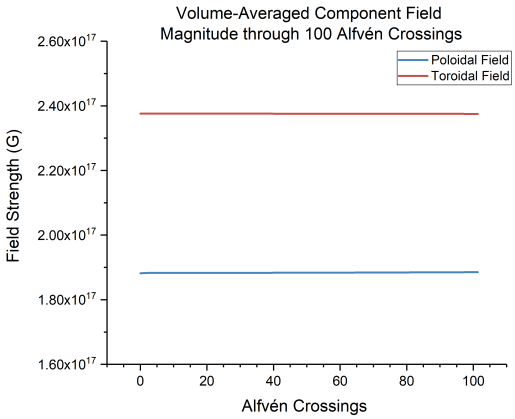

FIGURE 6.8: Volume-averaged magnitude of the poloidal and toroidal component fields through 100 Alfvén crossings. The fields remain near initial magnitude through Alfvén timescales.

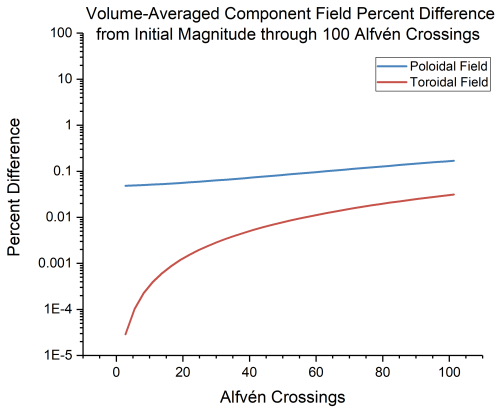

FIGURE 6.9: Percent difference evaluation for the poloidal and toroidal fields relative to initial configuration volume-averaged magnitude.

closely in Figure 6.9, where we plot the percent difference of each field from its initial $\bar{t}_A = 0$ magnitude up to $\bar{t}_A = 100$. Although the poloidal and toroidal fields vary slightly from their initial field strength, the low magnitude of their variation provides further supporting evidence for declaring our magnetic field configuration stable.

6.3 Numerical Estimates of Gravitational Wave Strain

6.3.1 Moment of Inertia Tensor Components I_{zz} & I_{xx}

In §**2.7**, we discuss the ellipticity, ϵ, and its relation to the gravitational wave strain, h_0 (equation (2.44)) produced by an asymmetrically rotating source such as a magnetar. In order to compute the ellipticity, we must first determine the inertia tensor components I_{zz} and I_{xx} and their evolution throughout the simulation.

Fortunately, our data visualization platform `VisIt` provides the user with various "queries" which can be used to analyze data, including computing the moment of inertia tensor. We determine I_{zz} and I_{xx} by evaluating the moment of inertia tensor in simulation time steps of 100 ms. Recall the the inertia tensor is formed from equation (2.46), which is a volume integral over the stellar interior. Thus, we anticipate numerical limitations on the accuracy of computed values for I_{zz} and I_{xx}, as

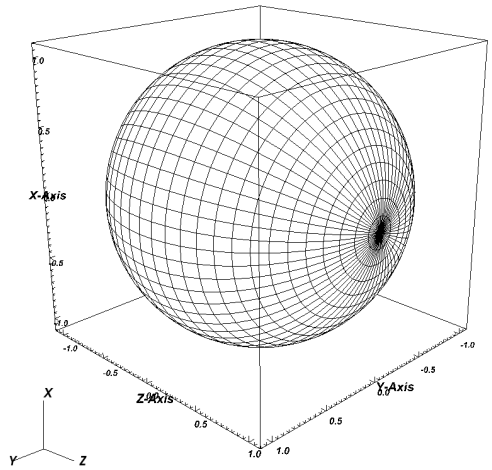

(A) I_{xx}: Integration along the x-axis

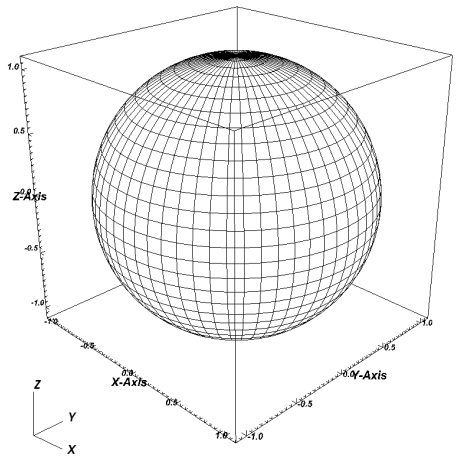

(B) I_{zz}: Integration along the z-axis

FIGURE 6.10: Configurations of the spherical mesh for integration of inertia tensor components. Evaluation of the I_{xx} component by integration along the x-axis is different than computation of I_{zz} along the z-axis

each tensor component must be computed over the discretized computational mesh of finite volume cells. Furthermore, because the spherical mesh is not uniform in both the polar angle θ and radially in r, calculation of I_{zz} by integrating along the z-axis results in a systematically different value than calculations of I_{xx} along the x-axis. Figure 6.10 illustrates the non-uniformity of the mesh along the x and z-axes, clearly indicating that the finite-volume mesh resolution systematically impacts numerical accuracy in computing the I_{xx} and I_{zz} inertia tensor components.

For the initial configuration of the stellar model at $t = 0$ s, the inertia tensor can be evaluated analytically as

$$I_{jk} = \int_V \rho(r, t = 0)\big(r^2\delta_{jk} - x_j x_k\big)dV \ , \tag{6.5}$$

where $\rho(r, t = 0)$ takes the form of equation (3.6a), such that

$$I_0 = I_{xx} = I_{yy} = I_{zz} = \frac{8(\pi^2 - 6)R^5\rho_c}{3\pi^3} \ . \tag{6.6}$$

From this analytic expression, we may determine the error in computing I_{zz} and I_{xx} via the difference between each numerically computed tensor component at simulation time $t = 0$ against the analytic expression (6.6). Figures 6.11 and 6.12 graph absolute error for I_{xx} and I_{zz}, respectively. In each plot, the radial resolution of the spherical mesh is kept constant while the angular resolution, measured by the number of discretizations along the polar axis, $n = \pi/d\theta$, varies from 10 to 70.

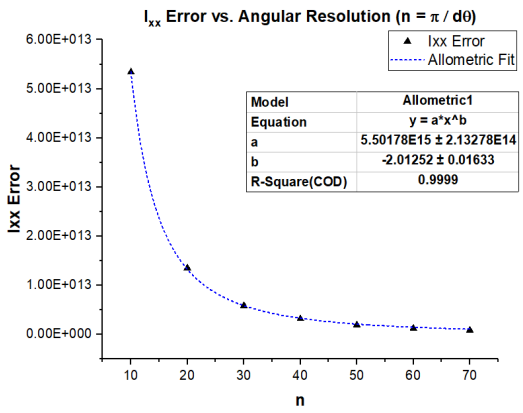

FIGURE 6.11: Allometric regression of I_{xx} absolute error vs angular resolution

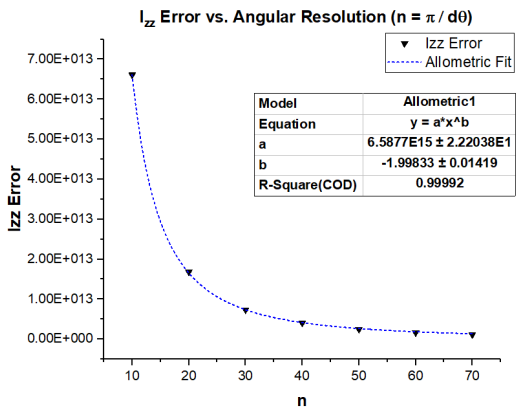

FIGURE 6.12: Allometric regression of I_{zz} absolute error vs angular resolution

We notice that the absolute error is proportional to $1/n^2$, with improvements to angular resolution affording less and less reduction in error for higher values of n. In §**7.1**, we discuss in more detail the impact of angular resolution on computation time, as this sets a constraint on our mesh resolution and thus the numerical precision of I_{xx} and I_{zz}.

Crucial to the evaluation of the ellipticity ϵ is the difference $I_{zz} - I_{xx}$, which we refer to as ΔI. Because the finite-difference integration scheme for these inertia tensor components over the spherical mesh provide slightly different values for $I_{zz}(t = 0)$ and $I_{xx}(t = 0)$, the value $|I_{zz}(t = 0) - I_{xx}(t = 0)| \neq 0$ is of considerable importance. This value, which we label δI_{zx}, represents a systematic error in our evaluation of I_{xx} and I_{zz}. Therefore, numerical evaluations for these tensor components take the following form

$$\begin{aligned} \boldsymbol{I_{xx}} &= I_{xx} \pm \delta I_{zx}(t = 0) \\ \boldsymbol{I_{zz}} &= I_{zz} \pm \delta I_{zx}(t = 0)\ . \end{aligned} \tag{6.7}$$

In Figure 6.13, we display the evolution over simulation time of $\boldsymbol{I_{xx}}$ and $\boldsymbol{I_{zz}}$ on the same graph for the instance of hydrostatic equilibrium where $|\boldsymbol{B}| = 0$. Both inertia components are assigned an error margin as expressed in equation (6.7), represented by the lighter shaded regions surrounding each curve. Because the error margins for both $\boldsymbol{I_{xx}}$ and $\boldsymbol{I_{zz}}$ overlap for the duration of the simulation, we strictly can not distinguish a non-zero value for the ellipticity, ϵ. For the instance of hydrostatic equilibrium, the null hypothesis is that I_{xx} and I_{zz} do not change from their

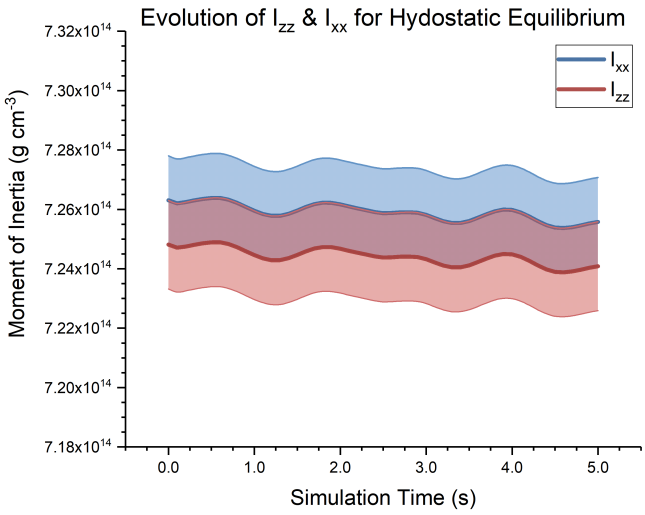

FIGURE 6.13: I_{zz} and I_{xx} evolution for conditions of hydrostatic equilibrium. The error margin δI_{zx} is represented by the shaded regions of each curve. The precise overlap of each error margin suggests that fluctuations in the inertia tensor are perfectly symmetric under hydrostatic equilibrium, and that the ellipticity remains zero throughout the duration of the simulation.

initial configuration, such that $I_{xx} = I_{zz}$ and $\epsilon = 0$. Thus, we trivially verify the null hypothesis for the instance of hydrostatic equilibrium. As an aside, we note that for Figures 6.13 and 6.14, the moment of inertia is given in g·cm^{-3} because the choice of normalized radius, $R = 1.0$, leaves expressions for the moment of inertia such as the analytic result of equation (6.6) with dimensions of density.

6.3.2 Ellipticity Measurements

For the non-trivial instance in which $\boldsymbol{I_{xx}}$ and $\boldsymbol{I_{zz}}$ evolve such that their error margins do not overlap, we can determine experimental measurements for ellipticity. We calculate error bounds for the ellipticity, where

$$\begin{aligned} \boldsymbol{\Delta I_{max}} &= (\boldsymbol{I_{zz}} + \delta I_{zx}) - (\boldsymbol{I_{xx}} - \delta I_{zx}) \\ \boldsymbol{\Delta I_{min}} &= (\boldsymbol{I_{zz}} - \delta I_{zx}) - \boldsymbol{I_{xx}} + \delta I_{zx}) \,, \end{aligned} \tag{6.8}$$

such that an experimentally determined ellipticity, $\boldsymbol{\epsilon}$, can be expressed as

$$\boldsymbol{\epsilon} = \frac{\boldsymbol{\Delta I}}{I_0} \pm \frac{2\delta I_{zx}}{I_0} \,. \tag{6.9}$$

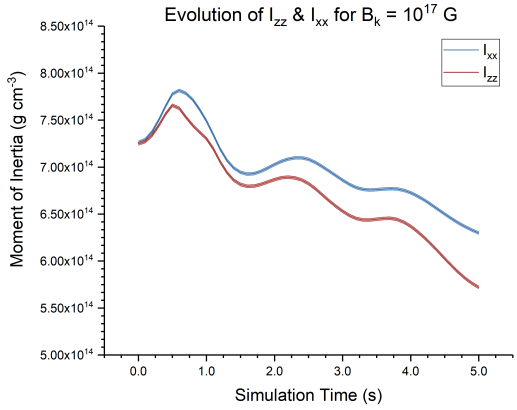

FIGURE 6.14: I_{xx} and I_{zz} evolution in the presence of a strong magnetic field. Notice that the inertia tensor components become distinctly separated, allowing measurement of ellipticity.

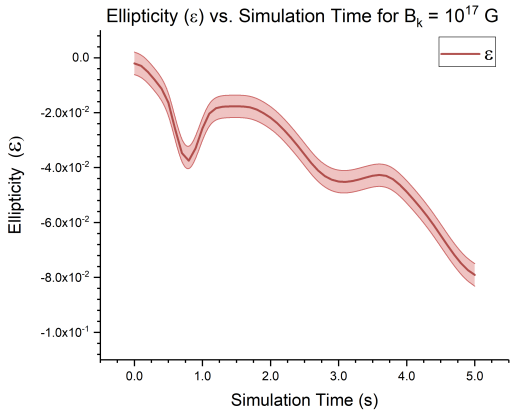

FIGURE 6.15: Ellipticity as measured for each instance of the evolution of I_{xx} and I_{zz} as depicted in Figure 6.14 in the presence of a magnetic field.

In Figure 6.14, we graph the evolution of $\boldsymbol{I_{xx}}$ and $\boldsymbol{I_{zz}}$ through a simulation time of $t = 5.0$ s where the magnetic field is assigned the magnitude $B_k = 1 \times 10^{17}$ G as discussed in §**4.4.2**. We notice a marked difference from the instance of hydrostatic equilibrium in Figure 6.13, as $\boldsymbol{I_{xx}}$ and $\boldsymbol{I_{zz}}$ become distinguishable such that measurements of ellipticity can be performed.

Recall that in §**2.7**, we suggested that the evolution of $\boldsymbol{I_{xx}}$ and $\boldsymbol{I_{zz}}$ may, given sufficient simulation time, approach stable values after initial variation due to reconfiguration of the stellar mass profile by the magnetic field. Our results in Figure 6.14 lead us to the conclusion that over the course of our simulation, $\boldsymbol{I_{xx}}$ and $\boldsymbol{I_{zz}}$ have yet to reach long term solutions. In Figure 6.15, we plot ellipticity computed for the above results of Figure 6.14. We notice that the value of the ellipticity becomes increasing negative, suggesting that the star becomes steadily more prolate with time. By simulation time $t = 5$s, we find the ellipticity to be $\boldsymbol{\epsilon} = (7.907 \pm 0.408) \times 10^{-2}$. Because $\boldsymbol{I_{xx}}$ and $\boldsymbol{I_{zz}}$ do not stabilize over the duration of the simulation, we set a provisional statement on our measurements of $\boldsymbol{\epsilon}$, such that the stable solution for the ellipticity, $\boldsymbol{\epsilon}^*$, lies below $\boldsymbol{\epsilon}(t = 5.0)$.

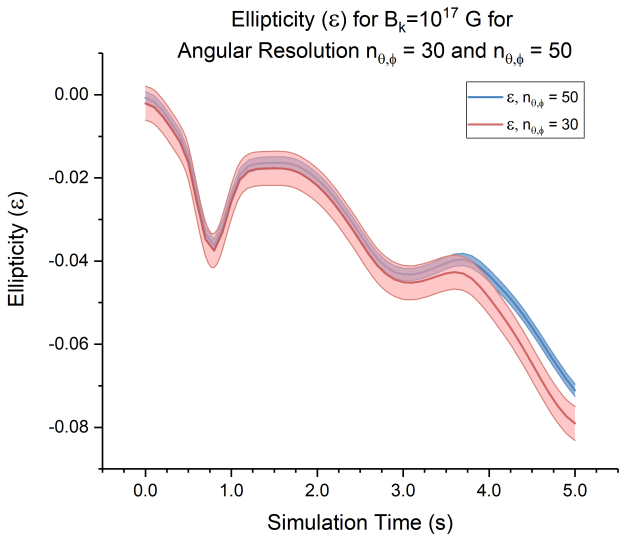

FIGURE 6.16: Comparison of ellipticity as calculated in Figure 6.15 (red) for angular resolution $n_{\theta,\phi} = 30$ and results for $n_{\theta,\phi} = 50$ (blue).

6.3.3 Effect of Angular Resolution on Ellipticity

We test the effect of increasing angular resolution of our simulation to determine whether greater mesh discretization modifies our calculation of ellipticity. We refer to angular resolution as the mesh discretization number density, $n_{\theta,\phi}$, in a hemisphere of both the polar and azimuthal grid. We increase angular resolution from $n_{\theta,\phi} = 30$ to $n_{\theta,\phi} = 50$ and find that for $t \lessapprox 3$ s, our results agree for both higher and regular resolution ellipticity measurements within error margins set by the ellipticity error margin expressed in equation (6.9). We plot our results in Figure 6.16.

For $t \gtrapprox 3$ s, we find that ellipticity measurement for higher angular resolution data trends marginally less negative than the regular resolution counterpart. These results suggests that increased angular resolution may result in ellipticity values which possess equilibrium configurations with absolute values below that of lower angular resolution results for ellipticity. We find that for $n_{\theta,\phi} = 50$, the ellipticity is $\boldsymbol{\epsilon}(t = 5.0) \approx 7.1 \times 10^{-2}$, which we utilize in **§6.3.4** and **§6.3.5** for gravitational wave strain calculations.

6.3.4 Upper-limit Estimate for h_0

In calculating upper limits for the gravitational wave strain, h_0, recall equation (2.44),

$$h_0 = \frac{4\pi^2 G}{c^4}\frac{I_0 f_{\rm gw}^2}{d}\epsilon\,, \tag{6.10}$$

where $f_{\rm gw} = 2/P$ is the gravitational wave frequency for P the period of rotation for the star and d is the distance from the observer to the gravitational wave source. We utilize average magnetar rotational period and stellar distance for stellar sources in the McGill Magnetar Catalog, where $P_{\rm avg} = 6.65$ s and $d_{\rm avg} = 11.43$ kpc, indicating that these are slowly rotating, galactic sources [2]. Utilizing fiducial values for neutron star parameters including unperturbed moment of inertia, I_0, we follow the work of Lasky in expressing wave strain as

$$h_0 = 4.2\times10^{-26}\left(\frac{\epsilon}{10^{-6}}\right)\left(\frac{P}{10\text{ ms}}\right)^{-2}\left(\frac{d}{1\text{ kpc}}\right)^{-1}\,, \tag{6.11}$$

where we formulate equation (6.10) such that we may easily determine wave strain via rotational periods in ms and distances in kpc [29]. Utilizing our determined value of $|\epsilon| \approx 7.1\times10^{-2}$ and average values for rotational period and distance via the McGill Magnetar Catalog, we find that

$$\bar{h}_0 \approx 4.2\times10^{-26}\left(\frac{7.1\times10^{-2}}{10^{-6}}\right)\left(\frac{6650\text{ ms}}{10\text{ ms}}\right)^{-2}\left(\frac{11.43\text{ kpc}}{1\text{ kpc}}\right)^{-1} \approx 5.9\times10^{-28}\,. \tag{6.12}$$

6.3.5 Strain Estimates for the McGill Magnetar Catalog

Recall via **§4.4.2** that our ellipticity calculation is determined for a magnetar with surface field strength $B_S \approx 2.5\times10^{15}$. Whereas average surface dipolar magnetic field strength $B_{\rm avg}$ for sources in the McGill Magnetar Catalog is $\sim 3.65\times10^{14}$ G and the maximum detected field strength $B_{\rm max}$ is 2.0×10^{15} G, our simulated surface field strength represents an upper limit on the existing set of known magnetar field strengths. Therefore, our determined value for ellipticity additionally represents an upper limit for known magnetar sources.

We compute upper limits of gravitational wave strain estimates for magnetars in the McGill Magnetar Catalog by utilizing equation (6.11) where we set ellipticity to our determined value,

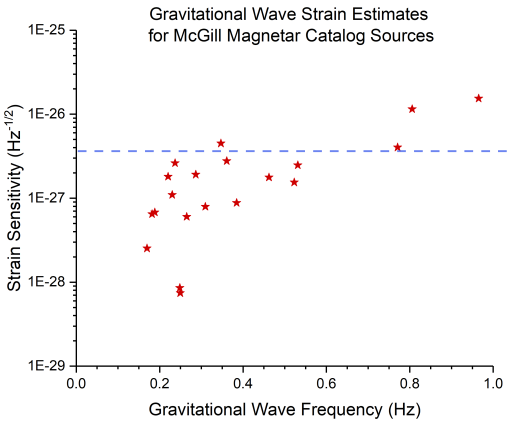

FIGURE 6.17: Wave strain estimates for sources in the McGill Magnetar Catalog computed via determined ellipticity simulations. The blue dashed line represents the average of computed wave strain values.

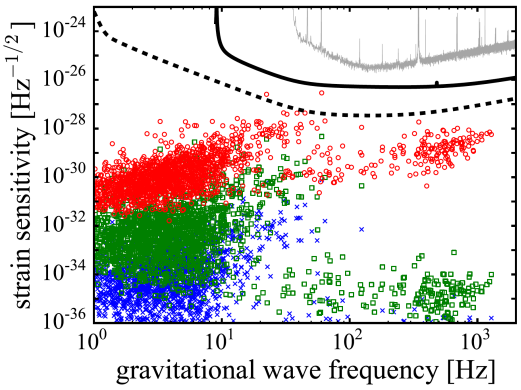

FIGURE 6.18: Wave strain predictions as calculated by Lasky [29]. The blue and red data represent estimates for ATNF pulsar catalog sources assuming purely poloidal and purely toroidal fields, respectively.

7.1×10^{-2}, and vary rotational period, P, and distance, d, in accordance with each source. We plot our results in Figure 6.17.

Lasky plots strain estimates for pulsars in the ATNF catalog, assuming stellar field configurations for purely poloidal fields in blue and near purely toroidal fields in green [29]. We find that our strain estimates for McGill Magnetar Catalog sources, assuming a mixed poloidal and toroidal magnetic field configuration, lie above (higher strain sensitivity) and to the left (lower wave frequency) of sources in Figure 6.18. Our results agree with intuition, as the comparatively stronger magnetic fields of magnetars will cause greater deformation and thus higher gravitational wave strain value. Unfortunately, because the slow rotational period of magnetars, we can not superimpose our data of Figure 6.17 onto Figure 6.18 given the mismatch in frequency domain.

We note that in Figure 6.18, Lasky plots various gravitational wave observatory detector strain sensitivity curves. The grey curve displays LIGO sensitivity for the initial S5 run, the black solid curve is the projected sensitivity of advanced LIGO (aLIGO) following various instrumentation upgrades, and the black dotted curve displays the sensitivity of the planned Einstein Telescope (ET). The operational frequencies of LIGO and aLIGO are limited on the low end to 10 Hz, and the frequency cutoff of ET is roughly 1 Hz. These limitations mean that present gravitational

wave observatories are not sensitive to continuous gravitational waves produced by slowly rotating magnetars; however, our results suggest that their wave strain may be in range of future detectors specializing in lower-frequency gravitational wave signals.

CHAPTER 7

CONCLUSION

7.1 Analysis of Results

In constructing a computational model for the stellar structure and magnetic field configuration of a magnetar, we have shown that our chosen stellar model, an $n = 1$ polytrope, remains at hydrostatic equilibrium via hydrodynamic simulations. Furthermore, we confirm that the mixed field configuration, combining both poloidal and toroidal component fields, is stable under Alfvén timescales. Thus, we confirm that the configuration of our model is structurally and dynamically stable.

We subsequently compute the stellar deformation due to the magnetic field as quantified by the ellipticity. Via measurements of stellar ellipticity, we compute upper-limit estimates for the gravitational wave strain for sources in the McGill Magnetar Catalog, a manifest of known magnetar sources. In comparing our results against prior gravitational wave strain predictions as computed by [29] for ATNF pulsar sources, we find that our results are in accordance with prediction; magnetars, possessing the strongest magnetic field strengths, will be deformed more than conventional pulsars by their respective fields, thus resulting in higher wave strain estimates.

Further work is required for analysis of ellipticity measurements, which inform our estimates for gravitational wave strain. We identify two primary sources of error which we seek to investigate. First, recall that determination of I_{zz} and I_{xx} are limited by the angular resolution of the computational mesh. In turn, we must introduce the error margin δI_{zx}, which limits the numerical precision for measurements of the ellipticity.

Figure 7.1 displays a log-log plot of the error term for the ellipticity against the angular resolution, which we label $n_{\theta,\phi}$ to indicate that the angular resolution is consistent in both the polar angle θ and the azimuthal angle ϕ. As we increase the angular resolution, the error term for ϵ decreases, although this comes at the cost of increased compute time for simulations. Figure 7.2

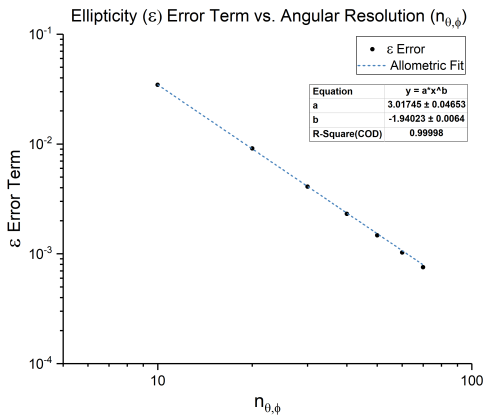

FIGURE 7.1: Log-log plot for the ellipticity error term against angular resolution.

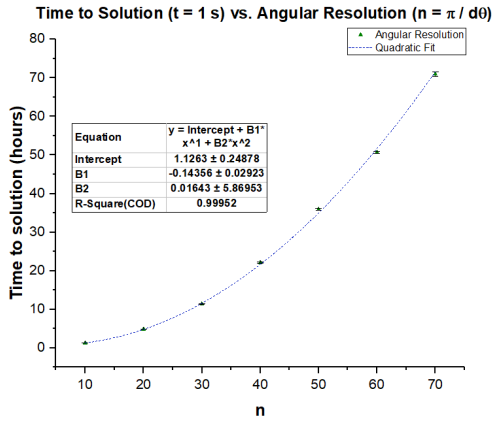

FIGURE 7.2: Quadratic regression of time to solution ($t = 1$ s) against angular resolution. Higher resolutions become increasing prohibitive in time duration.

displays a quadratic relationship between the angular resolution and time required to evolve the simulation by 1 second in computational time. We see that as the angular resolution increases, the compute time becomes increasingly prohibitive, which has presently limited our analysis to relatively short-term simulation duration up to $t = 5$ s. Simulations presented in this thesis have thus-far utilized only single-core computation, and extension to multi-core computing may significantly improve compute time and extend the range of feasible computational mesh resolutions for mitigating the ellipticity error margin.

We list a second source of error we wish to continue investigating. We find that the introduction of strong magnetic field strengths into our stellar model results in non-physical density evolution after $t \approx 3$ s. Figure 7.3 displays this phenomenon, which is characterized by abrupt changes in density distribution, and appears to be most pronounced along the polar axis and in the equatorial plane of the star. Because the density profile directly determines measurement of I_{zz} and I_{xx}, which inform the ellipticity and wave strain, correction of this seemingly spurious phenomenon is of key importance.

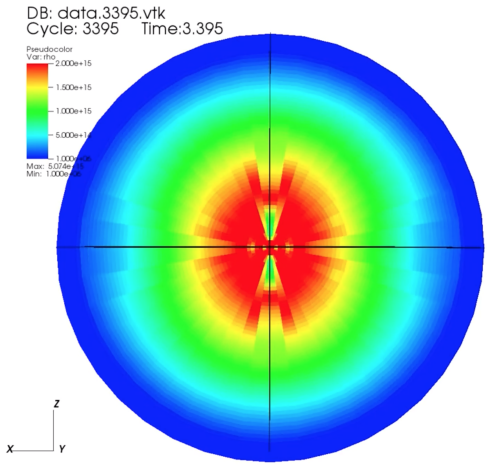

FIGURE 7.3: Pseudocolor plot of non-physical density phenomenon at simulation time $t = 3.395$ s. The localization along the polar axis suggests the issue may be related to polar boundary conditions.

7.2 Future Work

The work of this thesis allows numerous avenues for future study, as the field of research underpinning principle components of our findings provide a depth of opportunity in expanding this study to include more elaborate physical phenomena. In particular, we note important aspects of neutron star structure and computational methods which we note offer a greater degree of physical accuracy in modeling, however have been omitted from these results due to complexity and time constraints.

Here, we utilize the Newtonian formulation of hydrostatic equilibrium and mass conservation, which give way to the Lane-Emden equation for deriving structural expressions as a function of radius. The general relativistic correction to these equations comes in the form of the Tolman-Oppenheimer-Volkoff (TOV) equations. They may be solved in a similar manner to the Newtonian analog provided an equation of state (EOS). Although approximated fairly by a $n = 1$ polytrope, neutron star structure is varied and depends on a number of variables, not just density. A well celebrated EOS in neutron star physics is the SLy EOS, which is referred to as a "unified EOS" as transitions between structural regions including the outer and inner crust are computed via many-body calculation and thus preserve thermodynamic relations across boundaries [9].

We note that while the density, and thus mass, distribution of our stellar model evolve with time,

the gravitational is kept constant via the "Cowling Approximation". One may wish to implement a time-dependent gravitational potential in the form of a relativistic analog.

One may wish to include the contribution of non-ideal magnetohydrodynamic effects, such as the Hall effect and thermal diffusion [30].The influence of superconductivity has been shown to dramatically increase the scale of stellar deformations due to magnetic fields [1]. Thus, inclusion of its influence could improve estimates for continuous gravitational wave strain resulting from highly magnetic stellar sources.

Finally, we strongly recommend that determination of I_{zz} and I_{xx} should be investigated further to determine numerical integration schemes in 3-dimensional spherical coordinates which allow a high degree of accuracy via interpolation, while also supporting computational efficiency.

BIBLIOGRAPHY

BIBLIOGRAPHY

[1] B. Haskell et al. "Modelling magnetically deformed neutron stars". In: *Monthly Notices of the Royal Astronomical Society* 385.1 (2008), pp. 531–542. DOI: 10.1111/j.1365-2966.2008.12861.x.

[2] S. A. Olausen and V. M. Kaspi. "The McGill Magnetar Catalog". In: *The Astrophysical Journal Supplement Series* 212.1 (2014), p. 6. DOI: 10.1088/0067-0049/212/1/6.

[3] P. Haensel A.Y. Potekhin and D.G. Yakovlev. *Neutron Stars 1: Equation of State and Structure*. New York, NY: Springer, 2007. ISBN: 0-387-33543-9.

[4] Marguerite Holloway. *The Astronomer Jocelyn Bell Burnell Looks Back on Her Cosmic Legacy*. Jan. 2018. URL: https://www.newyorker.com/tech/annals-of-technology/the-astronomer-jocelyn-bell-burnell-looks-back-on-her-cosmic-legacy.

[5] Bradley W. Carroll and Dale A. Ostlie. *An Introduction to Modern Astrophysics*. Vol. 2nd Edition. San Francisco, CA: Pearson Addison Wesley, 2007. ISBN: 0805304029.

[6] A. M. Glazer and J. S. Wark. *Statistical mechanics: a survival guide*. Oxford Univ. Press, 2010.

[7] D. Lorimer and M. Kramer. *Handbook of Pulsar Astronomy*. Cambridge University Press, 2004.

[8] Van Horn H. M. *Unlocking the Secrets of White Dwarf Stars*. Springer, 2015.

[9] P. Haensel and A. Y. Potekhin. "Analytical representations of unified equations of state of neutron-star matter". In: *Astronomy Astrophysics* 428.1 (2004), pp. 191–197. DOI: 10.1051/0004-6361:20041722.

[10] Ta-Pei Cheng. *Relativity, Gravitation and Cosmology: A Basic Introduction*. Great Clarendon Street, Oxford: Oxford University Press, 2005. ISBN: 0-19-852957-0.

[11] B. P. Abbott et al. "GW170817: Observation of Gravitational Waves from a Binary Neutron Star". In: *Physical Review Letters* 119.161101 (2017), 161101.1 to 161101.18. DOI: 10.1103/PhysRevLett.119.161101.

[12] Emily Kuhn. "Magnetic Field Evolution in Magnetars with Gravitational Wave Applications". Duke University, 2016, Undergraduate Thesis.

[13] Alan J Weinstein. *Gravitational Waves and LIGO*. Dec. 2016. URL: https://www.slideshare.net/IanRothbarth/ligo-general-information?from_action=save.

[14] M.P. Hobson G. Efstathiou and A.N. Lasenby. *General Relativity: An Introduction for Physicists*. Great Clarendon Street, Oxford: Oxford University Press, 2006. ISBN: 0-521-82951-8.

[15] Michele Maggiore. *Gravitational Waves, Volume 1: Theory and Experiments*. Great Clarendon Street, Oxford: Oxford University Press, 2008. ISBN: 978-0-19-857074-5.

[16] David J Griffiths. *Introduction to electrodynamics; 4th ed.* Re-published by Cambridge University Press in 2017. Boston, MA: Pearson, 2013. URL: https://cds.cern.ch/record/1492149.

[17] Teviet Creighton. *Gravitational Waves: Formulae and details*. URL: http://www.tapir.caltech.edu/~teviet/Waves/gwave_details.html.

[18] Wayne Hu. *Quadrupole Types and Polarization Patterns*. 2001. URL: http://background.uchicago.edu/~whu/intermediate/Polarization/polar4.html.

[19] Hee-Suk Cho and Chang-Hwan Lee. "Analytical Calculation of the Mergers of Black Hole–Neutron Star Binaries". In: *Publications of the Astronomical Society of Japan* 62.2 (Jan. 2010), pp. 315–321. DOI: 10.1093/pasj/62.2.315. URL: http://pasj.asj.or.jp/v62/n2/620211/620211.html.

[20] Stan Woosley. *Lecture 7a: Polytropes*. Apr. 2014. URL: http://www.ucolick.org/~woosley/ay112-14/lectures/lecture7.14.pdf.

[21] Shijun Yoshida and Yasufumi Kojima. "Accuracy of the relativistic Cowling approximation in slowly rotating stars". In: *Monthly Notices of the Royal Astronomical Society* 289.1 (1997), pp. 117–122. DOI: 10.1093/mnras/289.1.117.

[22] I. W. Roxburgh. "Magnetostatic Equilibrium of Polytropes". In: *Monthly Notices of the Royal Astronomical Society* 132 (1966), pp. 347–358.

[23] E G. Flowers and M A. Ruderman. "Evolution of pulsar magnetic fields". In: *The Astrophysical Journal* 215 (June 1977), pp. 302–310.

[24] J. Braithwaite and H. C. Spruit. "Evolution of the magnetic field in magnetars". In: *Astronomy Astrophysics* 450.3 (2006), pp. 1097–1106. DOI: 10.1051/0004-6361:20041981.

[25] Hans Goedbloed and Stefaan Poedts. *Principles of Magnetohydrodynamics With Applications to Laboratory and Astrophysical Plasmas*. Cambridge University Press, 2004.

[26] Anne Greenbaum and Timothy P. Chartier. *Numerical Methods: Design, Analysis, and Computer Implementation of Algorithms*. Princeton University Press, 2012.

[27] Eleuterio F. Toro. *Riemann Solvers and Numerical Methods for Fluid Dynamics: A Practical Introduction*. second. Springer, 1999.

[28] Takeru Suzuki and Shigehiro Nagataki. "Alfven Wave-Driven Proto-Neutron Star Winds and r-Process Nucelosynthesis". In: *The Astrophysical Journal* 628 (Aug. 2005), pp. 914–922.

[29] Paul D. Lasky. "Gravitational Waves from Neutron Stars: A Review". In: *Publications of the Astronomical Society of Australia* 32 (2015). DOI: 10.1017/pasa.2015.35.

[30] Kotaro Fujisawa and Shota Kisaka. "Magnetic field configurations of a magnetar throughout its interior and exterior – core, crust and magnetosphere". In: *Monthly Notices of the Royal Astronomical Society* 445 (Sept. 2014).